Observation of large Rashba spin-orbit coupling at room temperature in compositionally engineered perovskite single crystals and application in high performance photodetectors

Abd. Rashid bin Mohd Yusoff,[1,*] Maria Vasilopoulou,[2] Arup Mahata,[3,4] Habib Ullah,[5] Bin Hu,[6] Wilson Jose da Silva,[7] Fabio Kurt Schneider,[7] Peng Gao,[8] Anton V. Ievlev,[9] Yongtao Liu,[9] Olga S. Ovchinnikova,[9] Filippo De Angelis,[4,10,*] Mohammad Khaja Nazeeruddin[11,*]

[1]Department of Physics, Vivian Tower, Singleton Park, Swansea University, SA2 8PP Swansea, United Kingdom

[2]Institute of Nanoscience and Nanotechnology (INN), National Center for Scientific Research (NCSR) "Demokritos", 15341 Agia Paraskevi, Attica, Greece

[3]CompuNet, Istituto Italiano di Tecnologia, Via Morego 30, 16163 Genova, Italy

[4]Computational Laboratory for Hybrid/Organic Photovoltaics (CLHYO), Istituto CNR di Scienze e Tecnologie Chimiche (SCITEC-CNR), Via Elce di Sotto 8, 06123 Perugia, Italy

[5]Environment and Sustainability Institute, University of Exeter, Penryn Campus, Penryn, Cornwall TR10 9FE, United Kingdom

[6]Department of Materials Science and Engineering University of Tennessee Knoxville, TN 37996, USA

[7]Universidade Tecnologica Federal do Parana, GPGEI – Av. Sete de Setembro, 3165 – CEP 80230-901, Curitiba, Parana, Brazil

[8]Fujian Institute of Research on the Structure of Matter, Chinese Academy of Science, Fuzhu, Fujian 350002, China

[9]Center for Nanophase Materials Sciences, Oak Ridge National Laboratory, Oak Ridge, TN, 37830 USA

Supporting Information

Observation of large Rashba spin-orbit coupling at room temperature in compositionally engineered perovskite single crystals and application in high performance photodetectors

Abd. Rashid bin Mohd Yusoff,[1,*] Maria Vasilopoulou,[2] Arup Mahata,[3,4] Habib Ullah,[5] Bin Hu,[6] Wilson Jose da Silva,[7] Fabio Kurt Schneider,[7] Peng Gao,[8] Anton V. Ievlev,[9] Yongtao Liu,[9] Olga S. Ovchinnikova,[9] Filippo De Angelis,[4,10,*] Mohammad Khaja Nazeeruddin[11,*]

[1]Department of Physics, Vivian Tower, Singleton Park, Swansea University, SA2 8PP Swansea, United Kingdom

[2]Institute of Nanoscience and Nanotechnology (INN), National Center for Scientific Research (NCSR) "Demokritos", 15341 Agia Paraskevi, Attica, Greece

[3]CompuNet, Istituto Italiano di Tecnologia, Via Morego 30, 16163 Genova, Italy

[4]Computational Laboratory for Hybrid/Organic Photovoltaics (CLHYO), Istituto CNR di Scienze e Tecnologie Chimiche (SCITEC-CNR), Via Elce di Sotto 8, 06123 Perugia, Italy

[5]Environment and Sustainability Institute, University of Exeter, Penryn Campus, Penryn, Cornwall TR10 9FE, United Kingdom

[6]Department of Materials Science and Engineering University of Tennessee Knoxville, TN 37996, USA

[7]Universidade Tecnologica Federal do Parana, GPGEI – Av. Sete de Setembro, 3165 – CEP 80230-901, Curitiba, Parana, Brazil

[8]Fujian Institute of Research on the Structure of Matter, Chinese Academy of Science, Fuzhu, Fujian 350002, China

[9]Center for Nanophase Materials Sciences, Oak Ridge National Laboratory, Oak Ridge, TN, 37830 USA

[10]Department of Chemistry, Biology and Biotechnology, University of Perugia, Via Elce di Sotto 8, 06123 Perugia, Italy

[11]Institute of Chemical Sciences and Engineering, École Polytechnique Fédérale de Lausanne (EPFL), Rue de l'Industrie 17, CH-1951 Sion, Switzerland

Email: abdr@khu.ac.kr, filippo.d.angelis@gmail.com, mdkhaja.nazeeruddin@epfl.ch

Supporting Note 1

Estimation of detectivity and responsivity. The key figure of merit that is usually employed in every type of photodetector is the specific detectivity D^*, which describes the smallest detectable signal. D^* can be viewed as a measure of the temporal noise in the photodetector and is defined through the following procedure: we first define the responsivity, R, as the ratio of photocurrent to incident light intensity that indicates how efficiently the detector responds to an optical signal. It is expressed as:

$$R = J_{ph}/L_{light} \qquad \text{(equation S1)}$$

where J_{ph} is the photocurrent density (equal to J_{total}-J_{dark}) and L_{light} is the incident light intensity. Then, the detectivity is given by:

$$D = 1/NEP\ (W^{-1}) \qquad \text{(equation S2)}$$

In equation S2, the noise-equivalent power (NEP) in watts as the incident flux required to give output voltage equal to the noise voltage: $NEP = V_n/R$ (watts), where V_n is the root-mean-square (RMS) noise voltage.

The specific detectivity, D^*, is the detectivity D for a 1-Hz bandwidth and a 1 cm^2 area:

$$D^* = D\ (A \times \Delta f)^{1/2} W^{-1} \text{cm. sec}^{-1/2} \qquad \text{(equation S3)}$$

D^* is independent of the detector area, A, and bandwidth, Δf, if the noise is proportional to $(A \times \Delta f)^{1/2}$. This area dependence is found if radiation fluctuations dominate the noise or if A is varied by connecting together several small identical detectors; the bandwidth dependence is found if the spectral response is flat over the relevant frequency range. The specific detectivity, D^*, is a normalized measure related to the inverse of the smallest signal that can be detected.

Supporting Note 2

Characterization of MoS_2. The frequency positions of E^1_{2g} and A_{1g} modes of our monolayer MoS_2 exfoliated on SiO_2/Si substrate are in good agreement with those previously reported for atomically thin layers (i.e. monolayer) with a slight red-shift compared to these values [1-3]. This can be explained by taking into account that when an atomically thin MoS_2 film is deposited onto a substrate, the lattice mismatch between thin film and substrate inevitably modifies the lattice of the thin film if they strongly interact. Large enough substrate-induced strain can be detected from Raman spectroscopy. For instance, uniaxial strain can cause an obvious red-shift for the E^1_{2g} mode and a small redshift for the A_{1g} mode [4]. The shift of the E^1_{2g} mode arises from the in-plane mode which can be largely affected by the substrate, while the small shift of the A_{1g} mode corresponds to the out-of-plane mode which is subject to smaller influence by the substrate. In our experiment, the lattice parameters of SiO_2 substrate are larger than that of MoS_2, which could supply a possible tensile strain on the monolayer MoS_2. However, a significant frequency shift of the E^1_{2g} mode has not been observed, which indicates that the monolayer MoS_2 endures only a small strain from the substrate, suggesting a very weak interaction between monolayer MoS_2 and the substrate. It is well known that monolayer MoS_2 is a direct band gap semiconductor and the quality and thickness of the crystal can be clearly assessed using PL measurements. In a photon-excited system, the exited electrons in the conduction band and holes in the valence band can bond together by virtue of electrostatic Coulomb force to form excitons. As one of the elementary quasi-particles describing the electronic response to optical excitation in solids, excitons are observed in monolayer MoS_2 PL spectra with two particular peaks associated with direct optical transitions from the lowest conduction bands to the highest spin-split valence bands [5]. In our experiment, one sharp PL peak at 1.85 eV (670 nm) and one broad peak at 2.0 eV (620 nm) match the A and B direct-gap optical transitions from the lowest conduction bands to the highest spin-split valence bands of MoS_2 [6,7]. The excellent optical quality confirms the monolayer thickness of MoS_2 and indicates their high crystal quality.

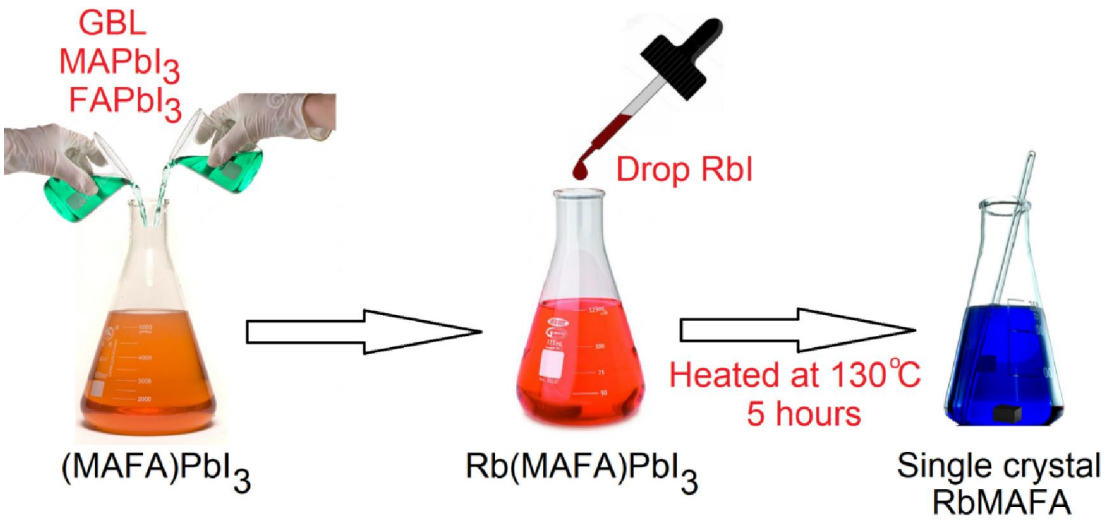

Figure S1 Synthetic procedure of the perovskite single crystals. Schematic illustration of the inverse temperature crystallization growth method used to fabricate the $Rb_x(MAFA)_{100-x}PbI_3$ (x=0, 5, 10 and 15) perovskite single crystals (SCs).

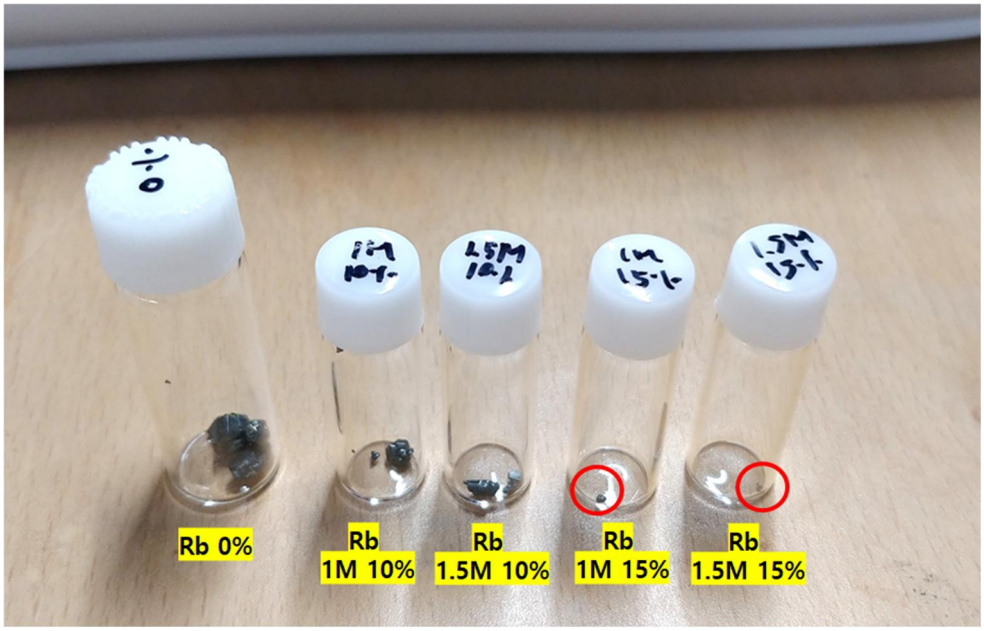

Figure S2 Photographs of the synthesized $Rb_x(MAFA)_{100-x}PbI_3$ (x=0, 10 and 15) perovskite SCs. The size of the developed SCs was dependent on the Rb doping ratio and overall solution concentration. The larger the Rb amount the smaller the crystal size.

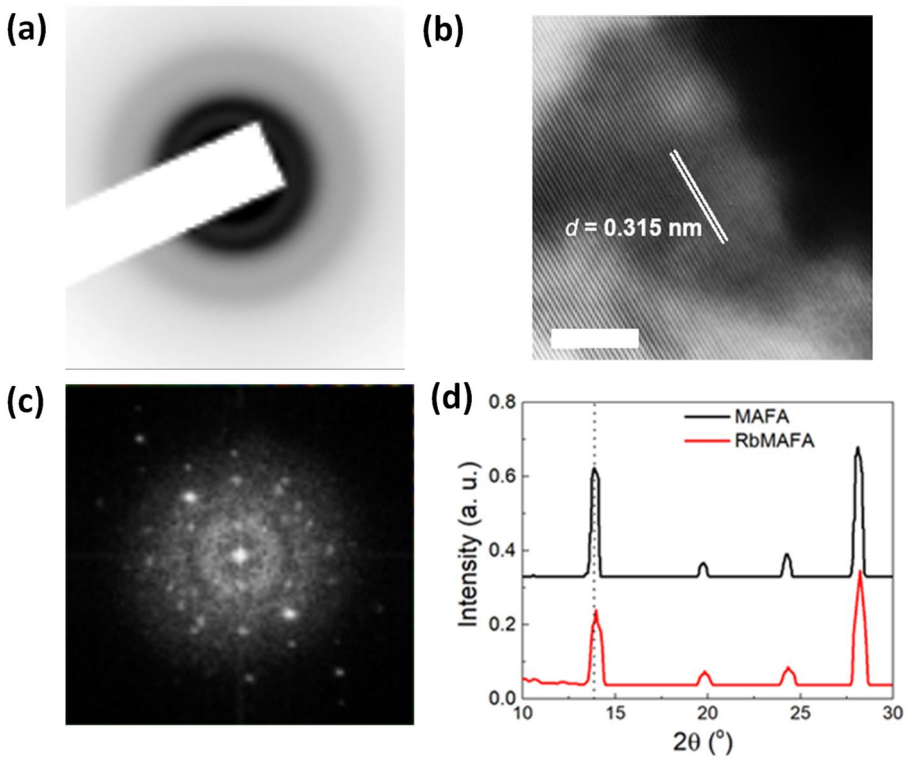

Figure S3 Structural properties of the 15% Rb perovskite single crystals. (a) Selective area electron diffraction (SAED) pattern and (b) high resolution transmission electron microscopy (HRTEM) image of a representative area of single crystals. (c) Low energy electron diffraction (LEED) patterns of a typical single crystal domain. (d) XRD patterns of RbMAFA (15% Rb) and MAFA (0% Rb) single crystals. (A zoom-in of these patterns is shown in Fig. 1b).

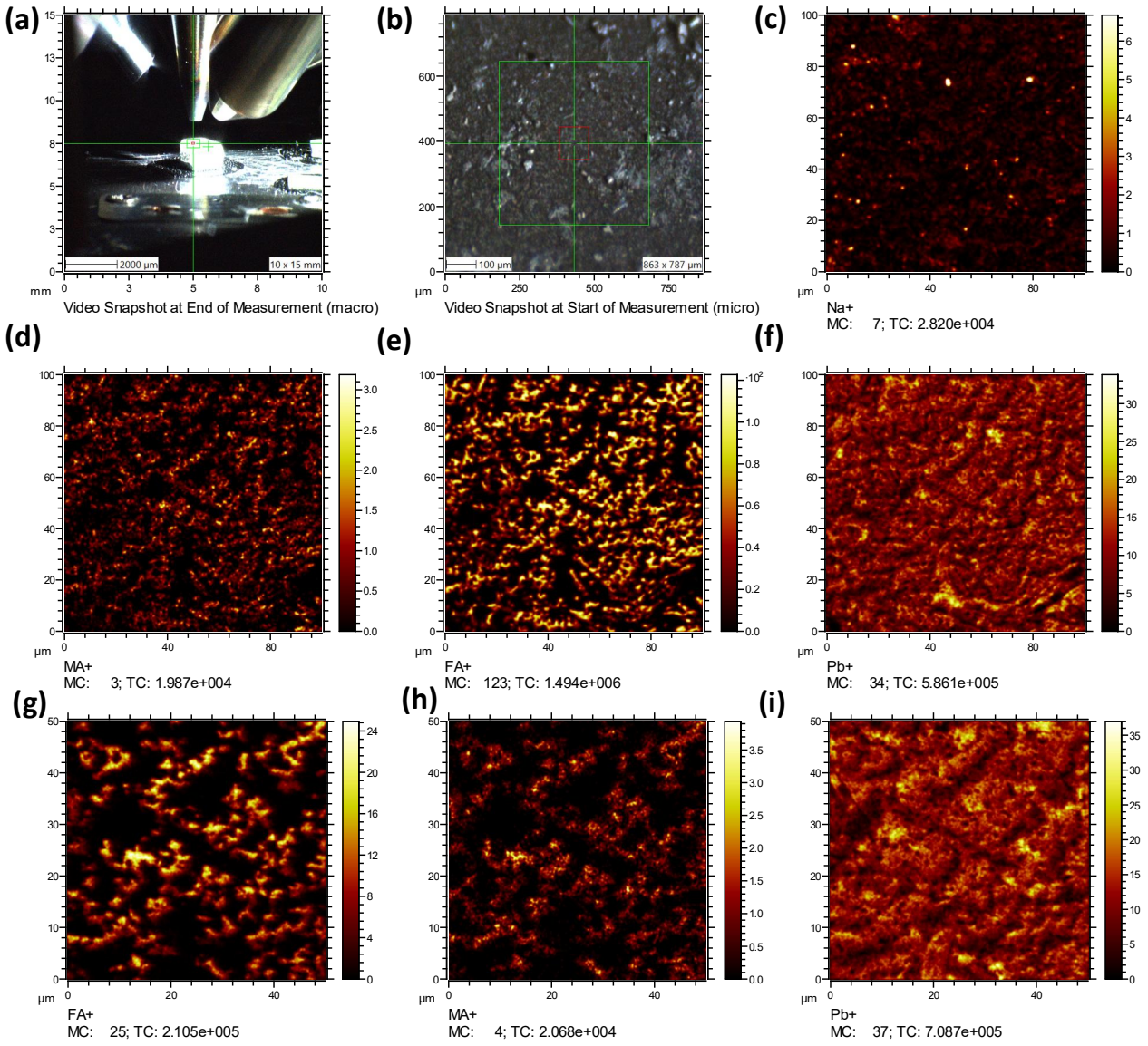

Figure S4 Time-of-Flight Secondary Ion Mass Spectrometry (TOF-SIMS) measurements of undoped perovskite single crystals. (a,b) Optical images and (c-f) TOF-SIMS images taken on the surface of 0% Rb MAFA perovskite single crystals. (g-i) TOF-SIMS measurements taken on the same sample crystal with a zoom-in of 50 µm.

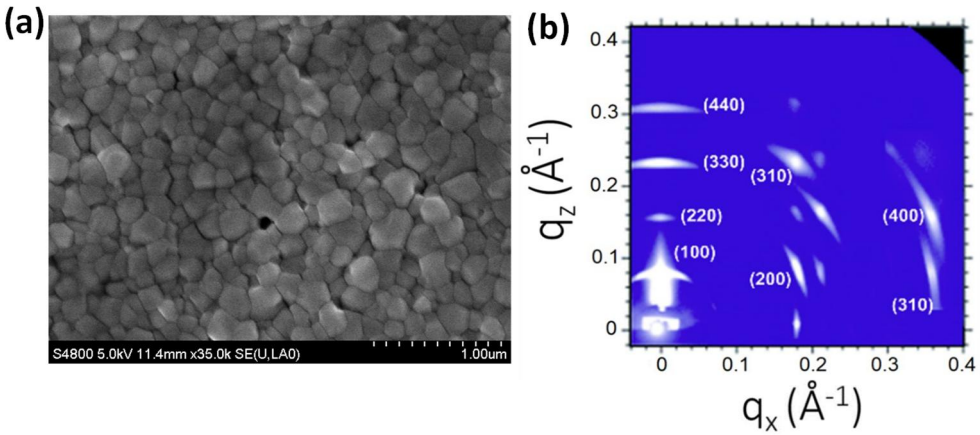

Figure S5 Morphology and structure of films printed from RbMAFA (Rb 15%) single crystals. (a) Scanning electron microscopy (SEM) topographic image of a perovskite film printed from 15% Rb single crystals. (b) 2D X-ray diffraction (XRD) pattern of a perovskite films prepared by direct printing from 15% Rb-doped single crystals. The high intensity of the (100) ring reveals that the film exhibits a preferential orientation.

.

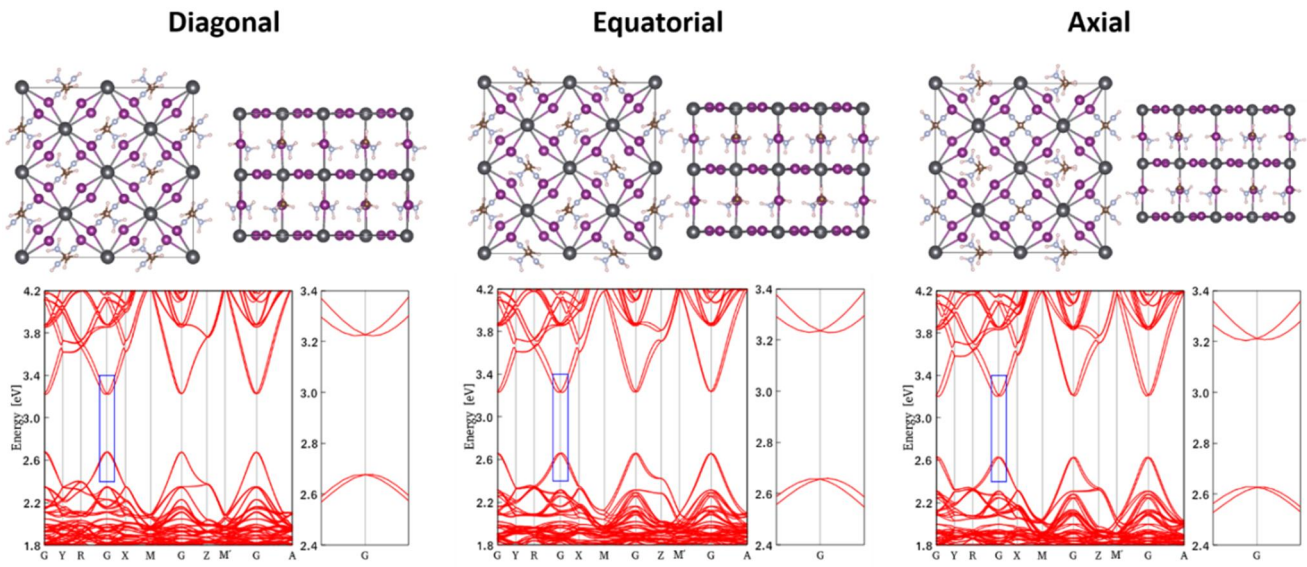

Figure S6 Theoretical prediction of Rashba spin-orbit coupling in MAFA (0% Rb) perovskite SCs. The different configuration of $MA_{0.5}FA_{0.5}PbI_3$ with respect to the position of MA and FA as summarized in Table S2. The diagonal, equatorial and axial configurations represent the position of MA and FA in a diagonal manner, alternate equatorial plane manner and alternate axial plane manner respectively.

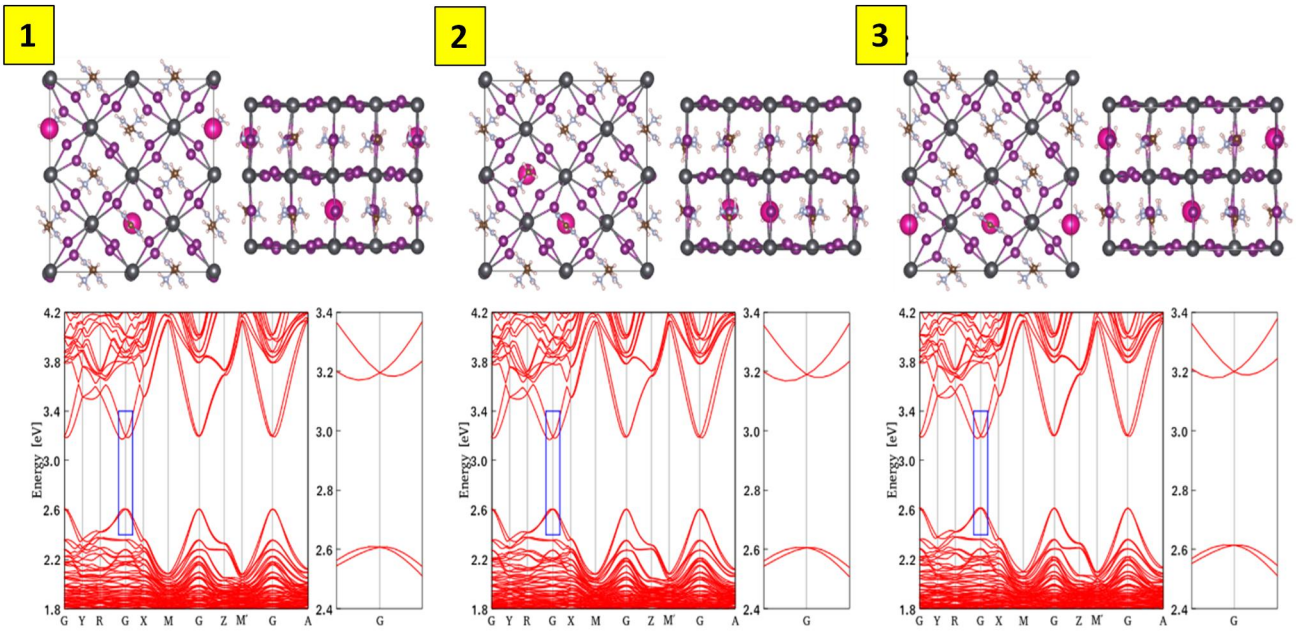

Figure S7 Theoretical prediction of Rashba spin-orbit coupling in RbMAFA (12.5% Rb) perovskite SCs. Different configuration of $Rb_{0.12}MA_{0.44}FA_{0.44}PbI_3$ with the variation of Rb-Rb distance as has been mentioned Table S3. The configurations are modelled by doping two Rb atoms in the base structure of diagonal $MAFAPbI_3$ in Figure S6.

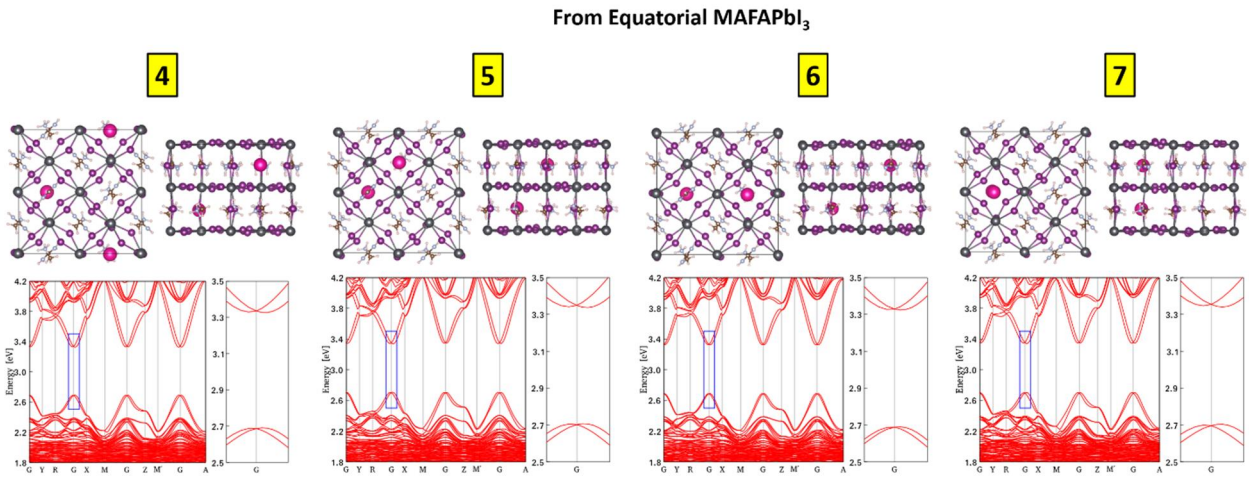

Figure S8 Theoretical prediction of Rashba spin-orbit coupling in RbMAFA (12.5% Rb) perovskite SCs. Different configuration of $Rb_{0.12}MA_{0.44}FA_{0.44}PbI_3$ with the variation of Rb-Rb distance as has been mentioned Table S3. The configurations are modelled by doping two Rb atoms in the base structure of equatorial $MAFAPbI_3$ in Figure S6.

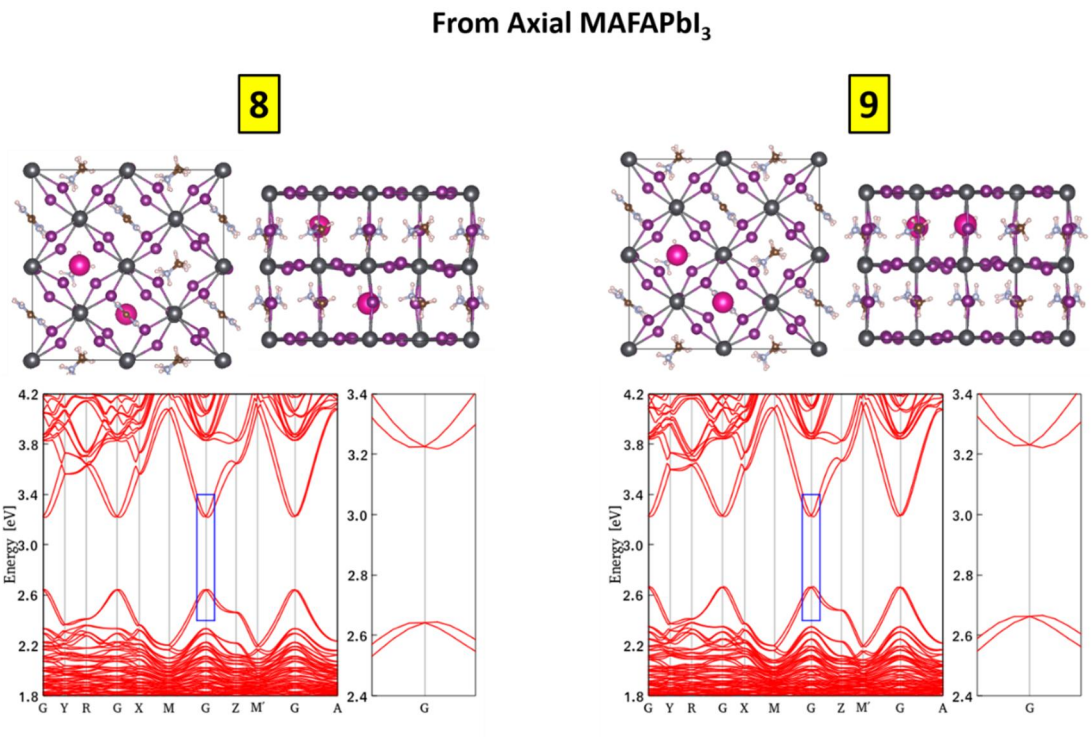

Figure S8 Theoretical prediction of Rashba spin-orbit coupling in RbMAFA (12.5% Rb) perovskite SCs. Different configuration of $Rb_{0.12}MA_{0.44}FA_{0.44}PbI_3$ with the variation of Rb-Rb distance as has been mentioned Table S3. The configurations are modelled by doping two Rb atoms in the base structure of axial $MAFAPbI_3$ in Figure S6.

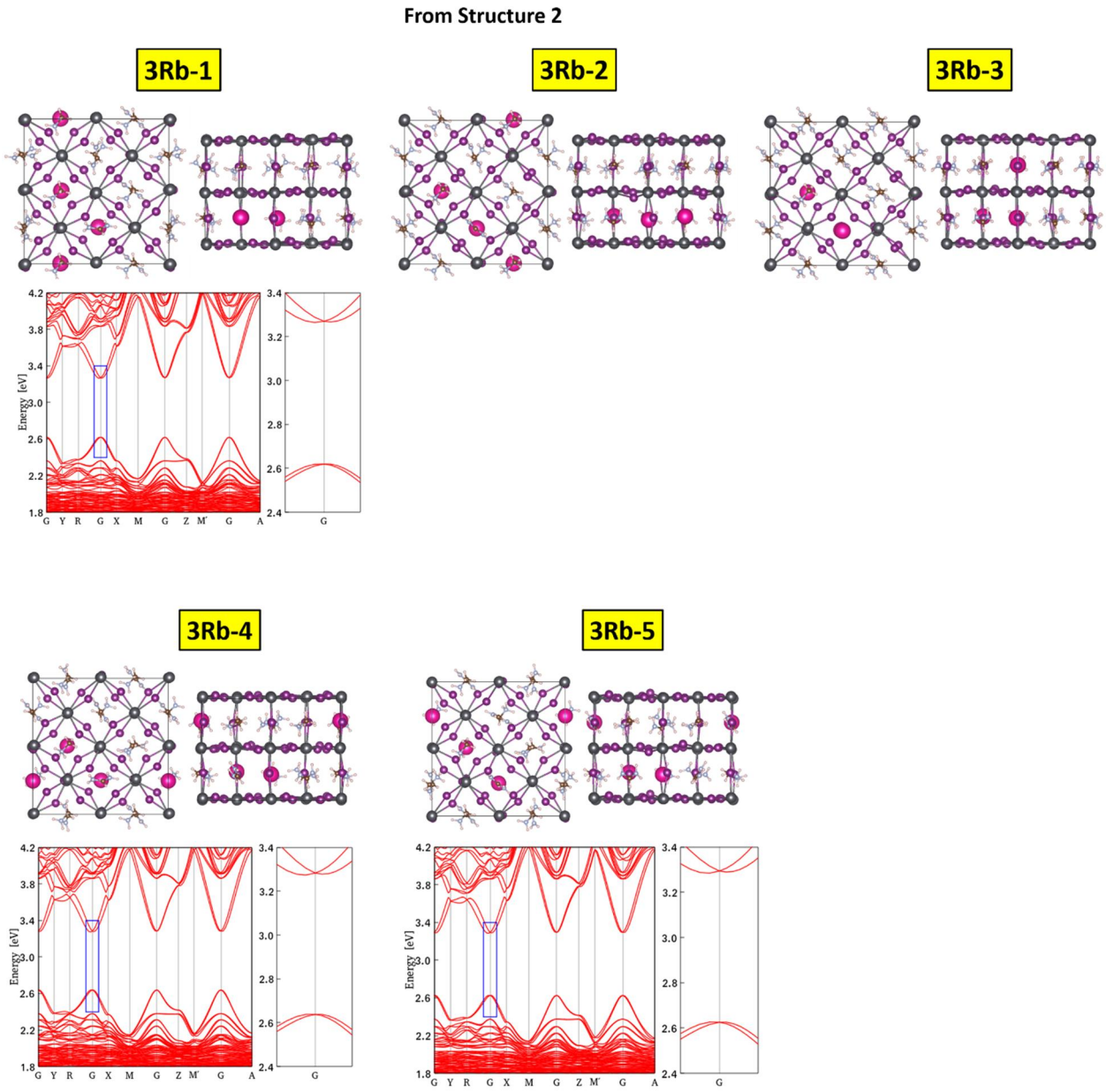

Figure S10 Theoretical prediction of Rashba spin-orbit coupling in RbMAFA (19% Rb) perovskite SCs. Different configuration of $Rb_{0.19}MA_{0.44}FA_{0.37}PbI_3$ with the variation of Rb-Rb distance as mentioned in Table S4.

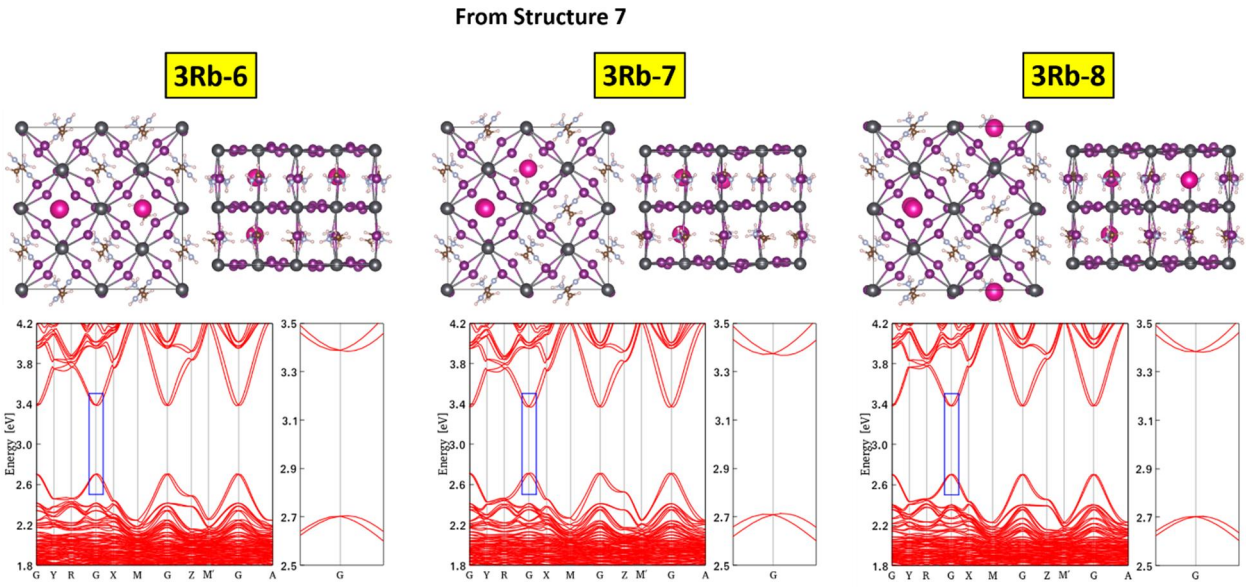

Figure S11 Theoretical prediction of Rashba spin-orbit coupling in RbMAFA (19% Rb) perovskite SCs. Different configuration of $Rb_{0.19}MA_{0.44}FA_{0.37}PbI_3$ with the variation of Rb-Rb distance as mentioned in Table S4.

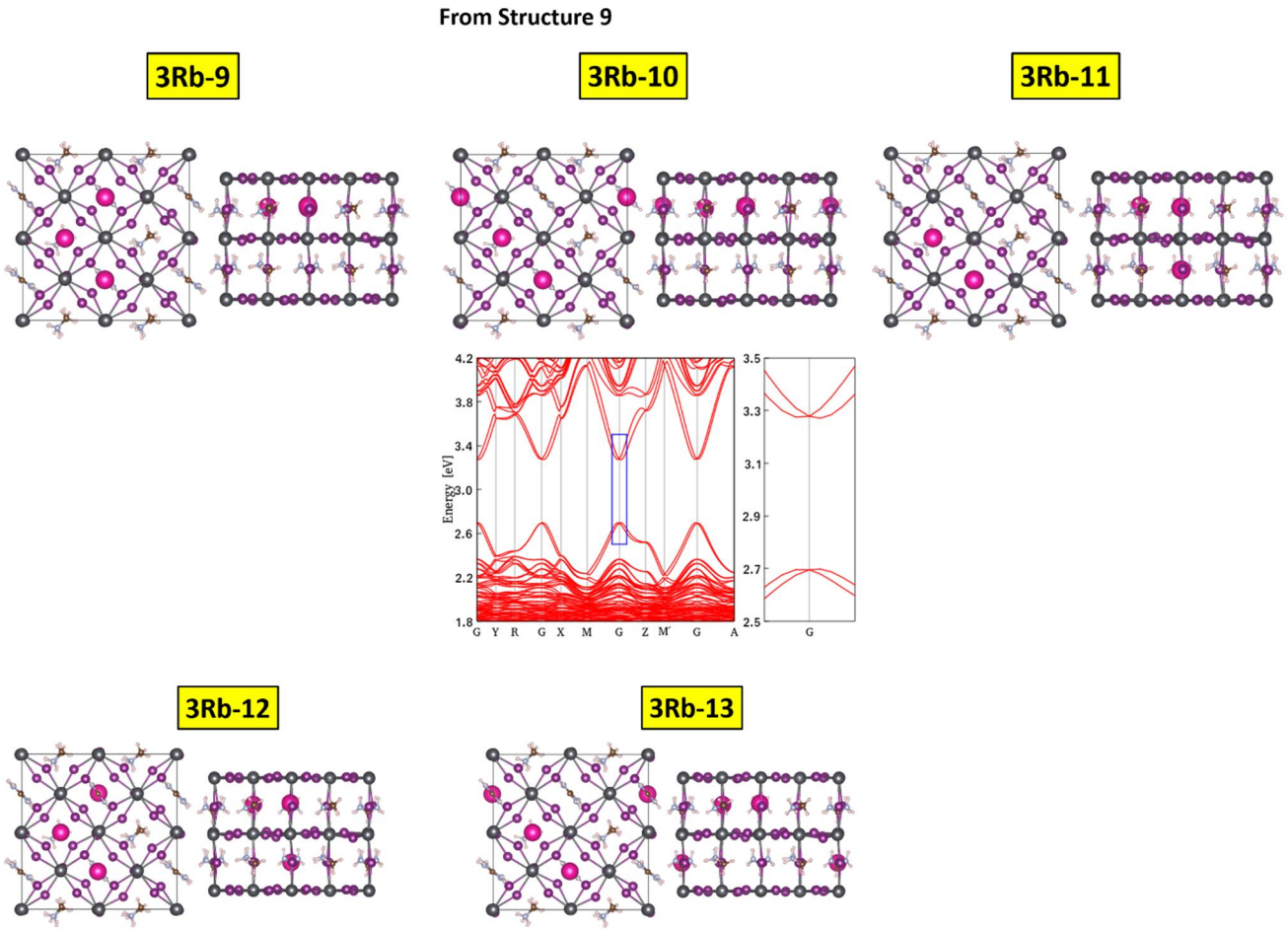

Figure S12 Theoretical prediction of Rashba spin-orbit coupling in RbMAFA (19% Rb) perovskite SCs. Different configuration of $Rb_{0.19}MA_{0.44}FA_{0.37}PbI_3$ with the variation of Rb-Rb distance as has been mentioned in Table S4.

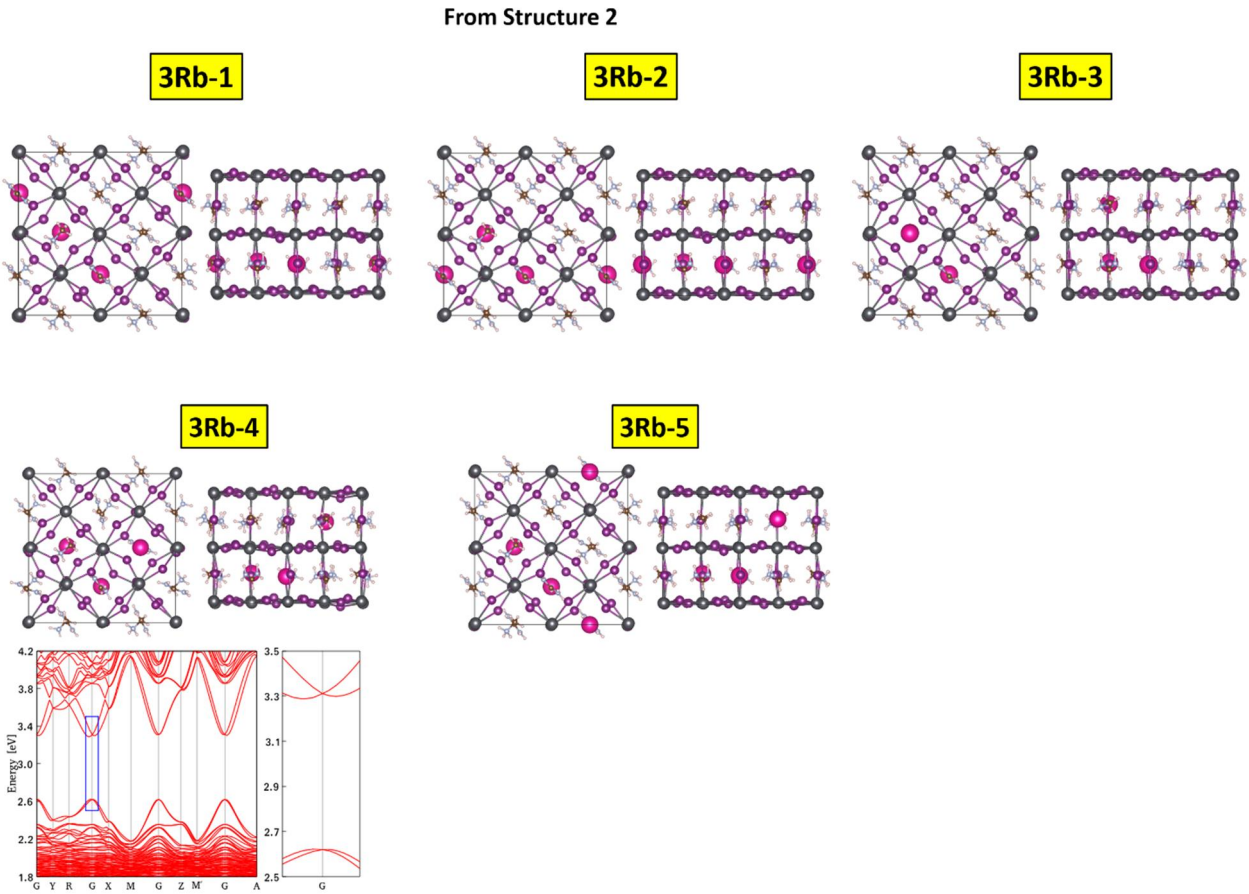

Figure S13 Theoretical prediction of Rashba spin-orbit coupling in RbMAFA (19% Rb) perovskite SCs. Different configuration of $Rb_{0.19}MA_{0.37}FA_{0.44}PbI_3$ with the variation of Rb-Rb distance as has been mentioned Table S5.

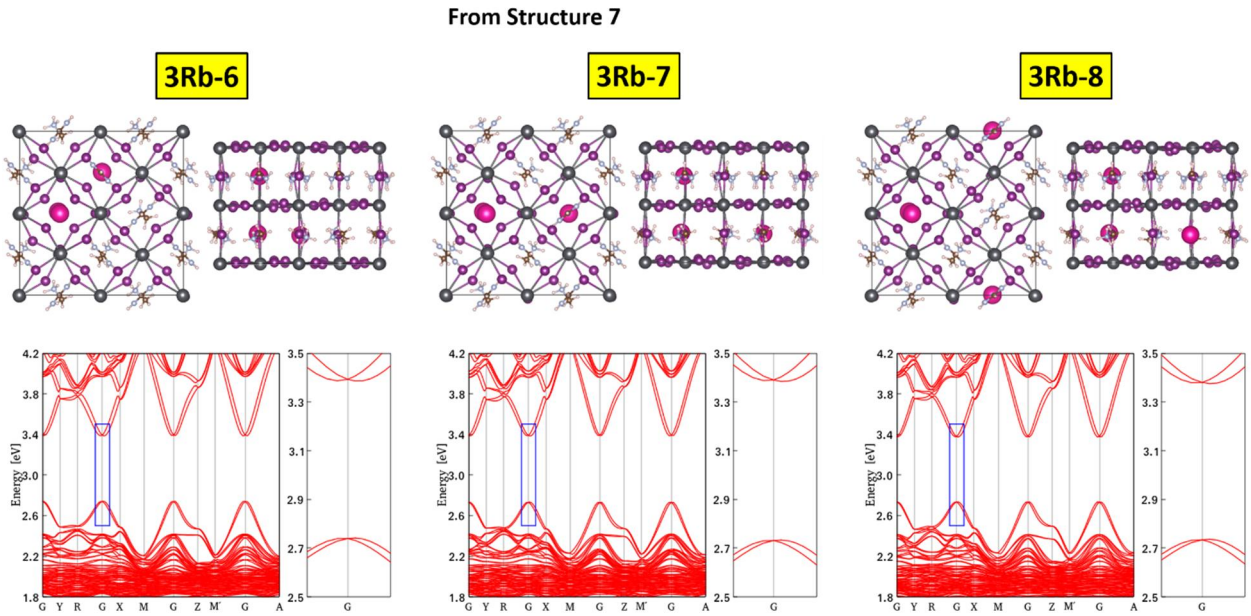

Figure S14 Theoretical prediction of Rashba spin-orbit coupling in RbMAFA (19% Rb) perovskite SCs. Different configuration of $Rb_{0.19}MA_{0.37}FA_{0.44}PbI_3$ with the variation of Rb-Rb distance as mentioned in Table S5.

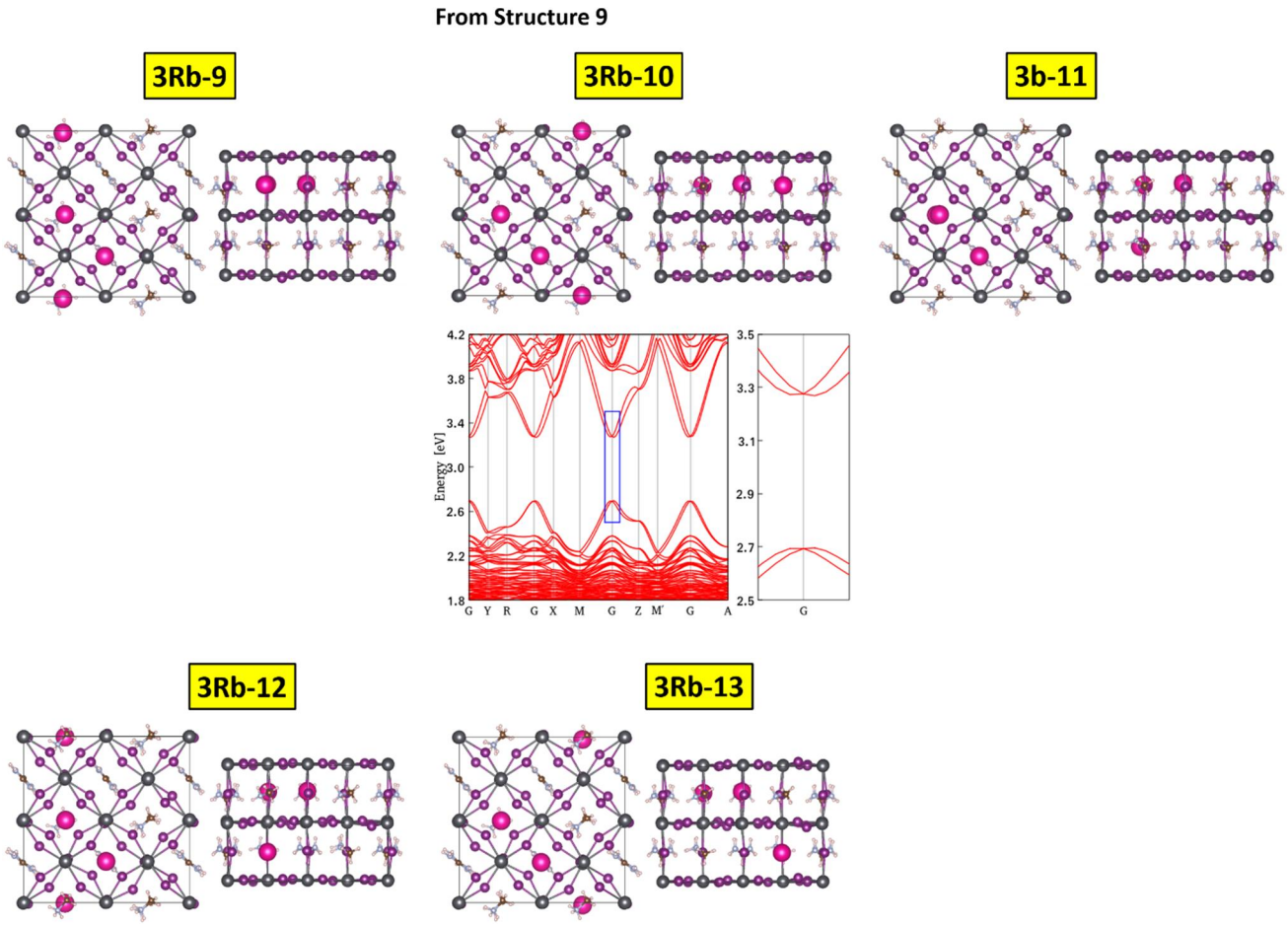

Figure S15 Theoretical prediction of Rashba spin-orbit coupling in RbMAFA (19% Rb) perovskite SCs. Different configuration of $Rb_{0.19}MA_{0.37}FA_{0.44}PbI_3$ with the variation of Rb-Rb distance as mentioned in Table S5.

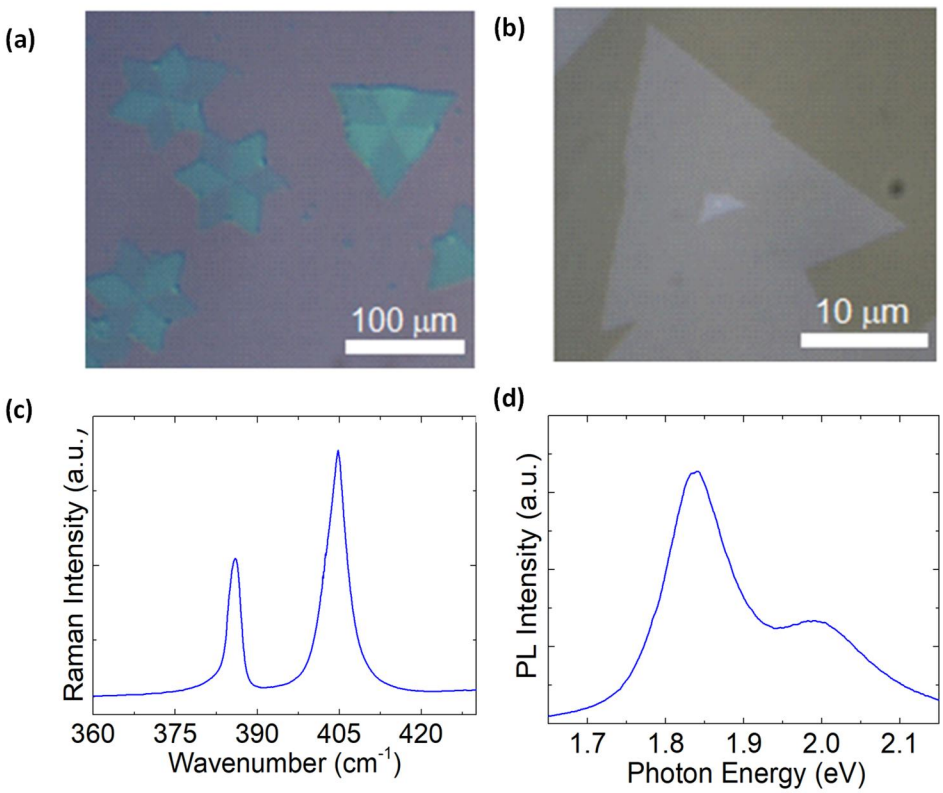

Figure S16 Morphological and structural properties of MoS_2 monolayer. SEM surface topography of (a,b) MoS_2 monolayer on SiO_2/Si substrate. (c) Raman spectra of monolayer MoS_2 on SiO_2 substrate. (d) Steady-state PL spectra of MoS_2 monolayer on SiO_2 substrate.

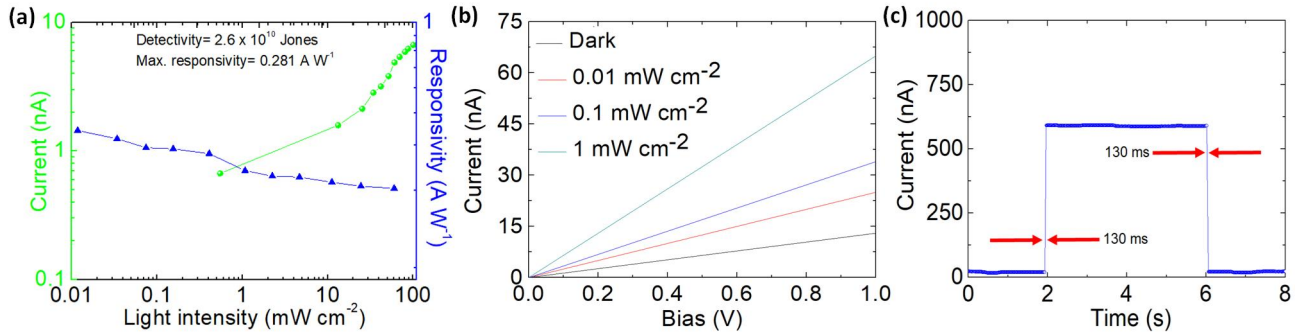

Figure S17 (a) Current and responsivity versus light intensity of a hybrid perovskite/MoS2 photodetector using MAFA (Rb 0%) single crystals. (b) I-V curves of the 15% Rb perovskite photodetector measured under low intensities of light. (c) 15% Rb photodetector rise/decay time. Temporal response of single-crystal perovskite photodetectors for the estimation of rise/decay time.

Table S1 TRPL fitting parameters. TRPL results and fitting parameters taken in perovskite films composed of $MAFAPbI_3$ (0% Rb) and $RbMAFAPbI_3$ (15% Rb) SCs. (TRPL results were fitted to a two-exponential decay: $A_1\exp(-t/\tau_1)+A_2\exp(-t/\tau_2)$, where $A_1+A_2=1$.)

Sample	**A_1**	**τ_1 (ns)**	**A_2**	**τ_2 (ns)**	**$\langle\tau\rangle$ (ns)**
$MAFAPbI_3$	0.17	5.28	0.86	54.46	46.34
$RbMAFAPbI_3$	0.09	7.48	0.93	88.48	81.33

Table S2. Rashba parameters of $MA_{0.5}FA_{0.5}PbI_3$ for the structures of Fig. S6. Δk, $\varepsilon^{\neq}$ and α represents the shift of valence and conduction band, band splitting energy, and Rashba interaction coefficient, respectively.

Systems	**Configuration**	**Relative Energy per f.u (meV)**	**Path**	**Δk (Å^{-1})**		**$\varepsilon^{\neq}$ (meV)**		**α (eV Å)**	
				VB	**CB**	**VB**	**CB**	**VB**	**CB**
$MA_{0.5}FA_{0.5}PbI_3$	Diagonal	10	G→R	0.005	0.013	2	19	0.15	0.69
			G→X	0.006	0.013	3	20	0.28	0.78
	Equatorial	3	G→R	0.008	0.017	5	28	0.30	0.84
			G→X	0.010	0.018	10	35	0.50	1.00
	Axial	0	G→R	0.009	0.012	7	34	0.36	0.94
			G→X	0.006	0.014	3	23	0.26	0.82

Table S3. Rashba parameters of $Rb_{0.12}MA_{0.44}FA_{0.44}PbI_3$ for the structures of Fig. 2 and Figs S7, S8.

Systems	Base Configu-ration	Structure (Closest Rb-Rb distance in Å)	Relative Energy per f.u (meV)	Path	Δk (Å^{-1})		$\varepsilon^{\neq}$ (meV)		α (eV Å)	
					VB	CB	VB	CB	VB	CB
$Rb_{0.12}$	From Diagonal	**1** (13.9)	34	G→R	0.009	0.036	4	117	0.24	1.62
				G→X	0.006	0.022	4	57	0.29	1.30
		2 (6.2)	30	G→R	0.009	0.034	4	104	0.22	1.55
				G→X	0.006	0.020	3	50	0.25	1.22
		3 (11.0)	32	G→R	0.008	0.033	3	102	0.20	1.53
				G→X	0.007	0.021	4	55	0.30	1.28
	From Equatorial	**4** (14.2)	7	G→R	0.009	0.015	6	24	0.34	0.77
				G→X	0.015	0.020	18	43	0.61	1.04
		5 (9.0)	4	G→R	0.013	0.019	13	32	0.49	0.86
				G→X	0.016	0.024	22	57	0.68	1.19
		6 (10.9)	9	G→R	0.006	0.011	2	13	0.19	0.58
				G→X	0.010	0.015	10	24	0.46	0.80

$MA_{0.44}FA_{0.44}PbI_3$		**7** (6.4)	0	G→R	0.013	0.018	12	30	0.47	0.83
				G→X	0.022	0.027	36	66	0.82	1.24
	From Axial	**8** (9.2)	22	G→M	0.009	0.011	5	14	0.29	0.63
				G→Z	0.011	0.016	10	35	0.42	1.11
		9 (6.1)	17	G→M	0.009	0.012	6	18	0.32	0.74
				G→Z	0.011	0.016	11	38	0.48	1.16

Table S4. Rashba parameters of $Rb_{0.19}MA_{0.44}FA_{0.37}PbI_3$ for the structures of Figs S9-S11.

Systems	Base Configu-ration	Structure (Closest Rb-Rb distance in Å)	Relative Energy per f.u (meV)	Path	Δk (Å^{-1})		$\varepsilon^{\neq}$ (meV)		α (eV Å)	
					VB	CB	VB	CB	VB	CB
	From Str 2	**3Rb-1** (6.3)	5	G→R	0.006	0.017	2	25	0.17	0.72
				G→X	0.005	0.012	2	14	0.19	0.60
		3Rb-2 (6.3)	32	-	-	-	-	-	-	-
				-	-	-	-	-	-	-
		3Rb-3 (6.3)	40	-	-	-	-	-	-	-
				-	-	-	-	-	-	-
		3Rb-4 (6.3)	1	G→R	0.008	0.022	4	43	0.23	0.98
				G→X	0.006	0.016	3	25	0.24	0.82
		3Rb-5 (6.3)	0	G→R	0.009	0.023	5	45	0.26	0.96
				G→X	0.006	0.015	4	23	0.28	0.77
		3Rb-6 (6.4)	24	G→R	0.004	0.006	0.6	3	0.07	0.23
				G→X	0.011	0.014	10	19	0.45	0.69

$Rb_{0.19}$ $MA_{0.44}FA_{0.37}PbI_3$	From Str 7	**3Rb-7** (6.3)	14	G→R	0.011	0.012	9	13	0.40	0.54
				G→X	0.016	0.019	22	34	0.66	0.91
		3Rb-8 (6.3)	26	G→R	0.005	0.008	1	5	0.13	0.34
				G→X	0.009	0.011	7	12	0.37	0.55
	From Str 9	**3Rb-9** (6.1)	32	-	-	-	-	-	-	-
				-	-	-	-	-	-	-
		3Rb-10 (6.2)	29	G→M	0.010	0.013	7	20	0.35	0.76
				G→Z	0.012	0.015	11	32	0.45	1.06
		3Rb-11 (6.2)	30	-	-	-	-	-	-	-
				-	-	-	-	-	-	-
		3Rb-12 (6.1)	30	-	-	-	-	-	-	-
				-	-	-	-	-	-	-
		3Rb-13 (6.1)	33	-	-	-	-	-	-	-
				-	-	-	-	-	-	-

Table S5 Rashba parameters of $Rb_{0.19}MA_{0.37}FA_{0.44}PbI_3$ for the structures of Figs S12-S15.

Systems	Base Configu-ration	Structure (Closest Rb-Rb distance in Å)	Relative Energy per f.u (meV)	Path	Δk (Å^{-1})		ε$^{\neq}$ (meV)		α (eV Å)	
					VB	CB	VB	CB	VB	CB
	From Str 2	**3Rb-1** (6.2)	35	-	-	-	-	-	-	-
				-	-	-	-	-	-	-
		3Rb-2 (6.2)	37	-	-	-	-	-	-	-
				-	-	-	-	-	-	-
		3Rb-3 (6.2)	33	-	-	-	-	-	-	-
				-	-	-	-	-	-	-
		3Rb-4 (6.2)	23	G→R	0.011	0.038	6	113	0.27	1.49
				G→X	0.008	0.025	4	59	0.29	1.18
		3Rb-5 (6.3)	37	-	-	-	-	-	-	-
				-	-	-	-	-	-	-
	From	**3Rb-6** (6.3)	0	G→R	0.008	0.018	4	25	0.23	0.76
				G→X	0.011	0.018	9	34	0.43	0.93
		3Rb-7 (6.3)		G→R	0.007	0.011	3	12	0.22	0.52

$Rb_{0.19}MA_{0.37}FA_{0.44}PbI_3$	Str 7		2	G→X	0.012	0.017	11	29	0.47	0.85
		3Rb-8 (6.4)	6	G→R	0.007	0.011	3	10	0.20	0.47
				G→X	0.012	0.015	11	23	0.47	0.77
	From Str 9	**3Rb-9** (6.1)	25	-	-	-	-	-	-	-
				-	-	-	-	-	-	-
		3Rb-10 (6.2)	21	G→M	0.010	0.012	7	17	0.35	0.70
				G→Z	0.012	0.015	11	30	0.45	1.00
		3Rb-11 (6.2)	26	-	-	-	-	-	-	-
				-	-	-	-	-	-	-
		3Rb-12 (6.1)	26	-	-	-	-	-	-	-
				-	-	-	-	-	-	-
		3Rb-13 (6.1)	26	-	-	-	-	-	-	-
				-	-	-	-	-	-	-

References

1. G. A. S. M. Buscema, H. S. J. van der Zant, A. Castellanos-Gomez, Nano Res. 7 (2014) 561–571.
2. C. Lee, H. Yan, L. E. Brus, T. F. Heinz, J. Hone, S. Ryu, ACS Nano 4 (2010) 2695–2700.
3. S.-L. Li, H. Miyazaki, H. Song, H. Kuramochi, S. Nakaharai, K. Tsukagoshi, ACS Nano, 6 (2012) 7381–7388.
4. C. Rice, R. J. Young, R. Zan, U. Bangert, D. Wolverson, T. Georgiou, R. Jalil, K. S. Novoselov, Phys. Rev. B: Condens. Matter. 87 (2013) 081307.
5. Y. Chen,. S. Huang, X. Ji, K. Adepalli, K. Yin, X. Ling, X. Wang, J. Xue, M. Dresselhau, J. Kong, B. Yildiz, ACS Nano 12(3) (2018) 2569–2579.
6. A. Splendiani, L. Sun, Y. Zhang, T. Li, J. Kim, C.-Y. Chim, G. Galli, F. Wang, Nano Lett.10 (2010) 1271–1275.

[10]Department of Chemistry, Biology and Biotechnology, University of Perugia, Via Elce di Sotto 8, 06123 Perugia, Italy

[11]Institute of Chemical Sciences and Engineering, École Polytechnique Fédérale de Lausanne (EPFL), Rue de l'Industrie 17, CH-1951 Sion, Switzerland

Email: abdr@khu.ac.kr, filippo.d.angelis@gmail.com, mdkhaja.nazeeruddin@epfl.ch

Abstract

Indirect absorption extended below the direct transition edge and increase in carrier lifetime derived from Rashba spin-orbit coupling may advance the optoelectronic applications of metal halide perovskites. Spin-orbit coupling in halide perovskites is due to the presence of heavy elements in their structure. However, when these materials lack an inversion symmetry, for example by the application of strain, spin-orbit coupling becomes odd in the electron's momentum giving rise to a splitting in the electronic energy bands. Here we report on the observation of a large Rashba splitting of 117 meV at room temperature through a facile compositional engineering approach in halide perovskite single crystals, as predicted by relativistic first-principles calculations. Partial substitution of organic cations by rubidium ions in single crystals induces significant indirect absorption and dual emission as a result of a large Rashba splitting. We measured significant magneto-photocurrent, magneto-electroluminescence and magneto-photoluminescence responses in perovskite single crystal devices and thin films. They originate from the significant spin-momentum locking that leads to different precession frequencies of their respective spins about the applied magnetic field. A hybrid perovskite single crystal photodetector achieved record figures of merit, including detectivity of more than 1.3×10^{18} Jones which represents a three orders of magnitude improvement compared to the to date record. These findings show that facile compositional

engineering of perovskite single crystals holds great promise for further advancing the optoelectronic properties of existing materials.

1. Introduction

Metal-halide perovskites of the general formula AMX_3, where A^+ is an organic or inorganic cation, M is a heavy metal such as Pb^{2+}, Sn^{2+} and X^- is a halide anion (Cl^-, Br^-, I^-), are in the forefront of current interest due to their salient features such as high absorption coefficient, long charge carrier diffusion length and low trap densities [1-3]. They are therefore considered of value in a variety of optoelectronic applications including solar cells [1-5], light-emitting diodes [6-8], memory devices [9,10] and photodetectors [11-27]. Spin-orbit coupling (SOC) related phenomena, such as the so-called Rashba effect, have recently gained much attention in perovskite systems as they induce intriguing optoelectronic phenomena, such as band gap narrowing and reduced non-radiative recombinations [28-31]. Large Rashba splitting is mostly observed in perovskite materials that exhibit pronounced spin-momentum locking upon breaking of the inversion symmetry as in the case of two-dimensional (2D) perovskites that form multiple quantum wells where the inversion symmetry is broken naturally. Recently, a significant (*i.e.* ~40 meV) Rashba splitting close to the extrema of the electronic bands has been reported for several 2D perovskites [32-34]. This splitting induces a direct-to-indirect band gap transition which is responsible for the observed band gap narrowing and for unusually long carrier lifetime. The latter is explained on the basis of the formation of an indirect band gap below the direct transition edge that protects thermalized carriers against recombination *via* the fast direct transition [35].

Generally weak Rashba splitting has been observed in three dimensional (3D) perovskite structures [36]. These are generally quasi-cubic centrosymmetric structures, which require the application of external forces such as strain to break their inversion symmetry [37-

39]. However, applying external pressure could be detrimental for practical applications. Despite the significant interest in Rashba effect related to fundamental knowledge, potential exploitation in applications requires facile methods to explore and possibly amplify this effect in perovskite materials and make use in practical devices. Intuitive strategies to achieve enhanced Rashba splitting and band gap modulation is to synthesize single crystals and/or vary the cation in A site [40]. Single crystals are prone to local inversion symmetry breaking due to structural disorder present in their surfaces [40]. Moreover, different A cation size and hydrogen bonding interactions in perovskite crystals and thin films may amplifying the effect of spin-orbit coupling through affecting the crystal structure [41].

Here, we manipulate at the atomistic level the geometric environment of the perovskite structure to achieve large Rashba splitting at room temperature through a facile compositional engineering approach applied in 3D perovskite single crystals. Substitution of methylammonium (MA) and formamidinium (FA) by an optimized fraction of rubidium (Rb) cations induces a Rashba splitting which causes red shifted indirect absorption, dual peak emission at room temperature and increase in the carrier lifetime by nearly a factor of two [28,38]. The magnitude of Rashba splitting was estimated by the energy difference of the emission peaks and found about 104 meV, which is consistent with the 117 meV calculated by first principles relativistic calculations. This is significantly higher compared to 35 meV which was predicted for the undoped perovskite single crystals. Our experimental evidence indicate uniform Rb substitution within the crystal surface and bulk whereas magnetic field effect measurements verify the enhanced odd-in-electron's momentum spin-orbit coupling. Our facile methodology of enhancing the Rashba splitting through compositional engineering of the perovskite single crystals enabled direct application in practical devices. Specifically, the Rb incorporated perovskite crystals served as an optoelectronic material platform to achieve high-performance photodetection in a perovskite/molybdenum sulfide (MoS_2) hybrid device

with detectivities exceeding 1.3×10^{18} Jones, nearly three orders of magnitude higher than the thus far reported record of 7.5×10^{15} Jones [11], demonstrating the potential impact of our approach in several classes of perovskite optoelectronics.

2. Results and discussion

Perovskite single crystals (SCs) of the general formula $Rb_x(MAFA)_{100-x}PbI_3$ (x=0, 5, 10, 15) were grown with an inverse temperature crystallization method in γ-butyrolactone (GBL) (Figure S1, Supporting Information (SI)). Compositional engineering was achieved through replacing part of MA and FA cations with Rb^+. The small radius alkali metal Rb^+ was chosen to replace some of the large organic cations in order to insert a symmetry changing structural distortion into the perovskite lattice aiming at breaking the crystal inversion symmetry [42]. This could induce enhanced Rashba splitting on the otherwise spin-degenerate parabolic bands [43,44]. The incorporation of Rb within the crystals, however, is challenging and it was accomplished by careful control of the temperature gradient whereas the crystals size was highly dependent on the Rb content. This was controlled through adjusting the precursor concentrations in the initial solution (Figure S2). The nominal stoichiometry of perovskite SCs that gave rise to both indirect absorption at room temperature and double peak PL emission was $Rb_{15}(MAFA)_{85}PbI_3$ (termed hereafter as RbMAFA for brevity). These crystals exhibited well-defined shape and size in the micrometer scale (Figure 1a). They were of fine quality as evidenced by the selective area electron diffraction (SAED), the low-energy electron diffraction (LEED) patterns, the high-resolution TEM (HRTEM) image and the X-ray diffraction (XRD) patterns (Figure S3a-d and Figure 1b). The crystal lattice of these crystals was affected by Rb incorporation as evidenced by the shift towards higher angles of the XRD peaks (Figure 1b). For the undoped crystals (termed hereafter as MAFA), the peak at 13.83° is attributed to (001) plane. This peak shifts to 13.94° for RbMAFA single crystals, which

indicates a small decrease in the lattice volume upon the incorporation of the smaller Rb^+ ion. Even a small lattice distortion, however, could be sufficient to induce enhanced Rashba splitting through breaking of inversion symmetry of the crystal [41,42,45]. Since X-ray diffraction represents a bulk analysis method, we speculate that Rb incorporation also proceeds within the bulk and it is not only limited in the surface of the crystals. To unravel, however, if this incorporation uniform, we performed elemental analysis in the MAFA and RbMAFA SCs using time-of-flight secondary ion mass spectrometry (TOF-SIMS) measurements. The TOF-SIMS profiles verified that there are no Rb cations in the undoped samples, while Rb cations are incorporated into the perovskite lattice quite uniformly and do not form aggregates in the interspace. This was further corroborated by TOF-SIMS images that show the surface (Figure 1e,f) and the inner within 50 μm zoom-in (Figure 1g,h) of the RbMAFA samples. Similar measurements were obtained in the undoped samples (Figure S4). It becomes evident that Rb incorporates homogeneously on the surface and inside the lattice of the doped crystals. This was also supported by electron dispersion spectroscopy (EDS) (Figure i-l). As a result, we expect that with our method we are able to induce compositional tuning within the bulk and surface of these crystals.

Next, we were able to deposit printable perovskite films of high quality from these crystals using a doctor blade technique (Figure S5). Figure 2a presents the UV-Vis absorption spectrum of a perovskite film deposited from RbMAFA SCs. Remarkably, the absorption spectrum extends far into the near-infrared region with the absorption onset reaching ~900 nm. This extension in the absorption onset is surprising, as incorporation of smaller Rb cations should induce band-gap opening due to structural distortion [46,47]. The observed absorption shift can be attributed to either gap states lying below the bands extrema or to indirect tail states lying below the indirect transitions [48-50]. However, trap states cause undesirable recombinations hence decreasing carrier lifetime. Transient photoluminescence (TRPL) decay

curves measured at room temperature in films composed of RbMAFA and MAFA SCs (Figure 2b) indicate a strong increase in carrier lifetime in the 15% Rb-doped SC films. The TRPL were fitted with two exponentials each and the fitting parameters and estimated carrier lifetimes are summarized in Table S1. A nearly 100% enhancement in carrier lifetime of RbMAFA compared to MAFA perovskite (from 46.34 to 81.33 ns) denotes that the below band gap transitions in the compositionally engineered perovskite are not likely to originate from trap states as they would decrease the charge carrier lifetime. Further evidence for the existence of strong indirect transitions in the Rb-engineered perovskite SCs were obtained by the room temperature steady-state PL spectrum taken in films composed of RbMAFA SCs (Figure 2c). Remarkably, the PL spectrum presents dual emission consisting of a main peak centered at 762 nm (1.627 eV) and a second, weaker but distinct peak at 814 nm (1.523 eV). Recently, Wang et al. [28], and Grätzel and co-workers [38], attributed the dual peak PL to the direct and indirect band gap emission in $MAPbI_3$ films and $APbBr_3$, where A corresponds to caesium, MA or FA, single crystals, respectively. The indirect band gap was originated from enhanced Rashba splitting upon breaking the crystal centrosymmetry. Similar direct and indirect dual emission peaks have also been reported in conventional indirect semiconductors such as germanium (Ge), gallium selenide (GaSe), and 2D transition metal dichalcogenides (MoS_2, $MoSe_2$) [51,52]. We therefore believe that our results indicate a significant Rashba splitting in the Rb-engineered perovskite SCs which causes the formation of tail states with an exponential distribution below the direct band gap. The effect should be stronger at the conduction band minimum (CBM) because the atomic number of Pb (Z = 82), the orbitals of which have major contribution in the conduction band minimum, is larger than I (Z = 53). We calculated the energy Rashba splitting from the energy difference between the two peaks in the dual peak PL spectrum of RbMAFA SC film and found it to be ~104 meV.

To confirm the existence of spin-dependent splitting, we applied a magnetic field to induce spin precession and studied spin-dependent optoelectronic characteristics in single crystal perovskite films and devices. The device included a perovskite film inserted between a ferromagnetic (NiFe) and a silver electrode. We expected that the applied magnetic field will modulate the optoelectronic properties of both films and devices. If Rashba splitting is indeed present in our crystals, the large spin-orbit coupling will become odd in the electron momentum. Through the magnetic field we induce changes in the spin-momentum pair with different spin configurations thus changing the photoluminescence/electroluminescence emission intensity or the device photocurrent [53,54]. Our measurements indicate that magneto-photoluminescence taken in films, magneto-electroluminescence and magneto-photocurrent taken in the complete device are highly dependent on the magnitude of the applied magnetic field (Figure 2d-f). When the magnetic field is applied in the presence of large Rashba splitting, spin precession takes place with a field and the spin-polarized electrons modulate the measured film/device emission/current [55]. We observe that magneto-electroluminescence appears with opposite polarity compared with that of magneto-photoluminescence and magneto-photocurrent. This is because magneto-electroluminescence originates from electron-hole pairs formed upon carrier injection that should be both triplet and singlet in nature with a ratio 3:1. In contrast, magneto-photoluminescence in the perovskite film and magneto-photocurrent in the complete device come from electron-hole pairs generated after photon absorption and present solely in the singlet configuration. This explains their similar polarity that is opposite to that of magneto-electroluminescence.

Our experimental results indicated that due to a non-centrosymmetric crystal environment upon Rb doping, spin-polarized bands whose minima are shifted in momentum space are present in RbMAFA crystals (Figure 3a). The figure of merit of the Rashba effect is in this case defined as the Rashba interaction parameter, α. To investigate the effect of

structural distortion introduced in the perovskite host by Rb incorporation, we carried out relativistic Density functional theory (DFT) calculations on (MAFA)PbI_3 and on $Rb_x(MAFA)_{1-x}PbI_3$ perovskites based on 2×2×1 supercell containing 16 formula units [56-60]. We start by investigating the 50:50 MAFA perovskite experimentally characterized considering various mutual positions of MA and FA molecules. We found three representative structures which are very close in energy (within 10 meV per formula unit) characterized by a small Rashba parameter (Figure 3b, Figure S6 and Table S2), suggesting a small inversion symmetry breaking due to the size mismatch between MA and FA cations. Starting from these three parent structures, we investigate the effect of 12.5% Rb incorporation, close to the nominal 15% Rb doping experimentally introduced. We have performed an extended structural sampling of all the possible geometries corresponding to the specific Rb doping, finding overall nine possible structures whose energy is within 34 meV, Figure 3 and Figs S7-S9 and Table S3. It is interesting to notice that for each of the Rb-containing structures a higher α value than the corresponding parent structures is predicted, clearly indicating that incorporation of Rb ions strongly enhances the Rasha effect in the considered perovskite host. As an example, for the most stable RbFAMA structure the Rashba interaction parameter increases from 1.00 to 1.24 eV Å compared to the parent MAFA structure, while maximum values of 1.00 and 1.62 eV Å are found considering slightly less stable FAMA and RbFAMA structures, respectively, see Figure 3 and Table S3. We have stepped forward to investigate the Rashba effect with higher Rb concentration by doping three Rb atoms in the same supercell, thus modeling the composition $Rb_{0.19}MA_{0.44}FA_{0.37}PbI_3$ and $Rb_{0.19}MA_{0.37}FA_{0.44}PbI_3$. Optimized geometries, energetics and Rashba parameters for these configurations have been reported in Figs S10-S15 and Tables S4 and S5. Notably, further Rb addition does not generally lead to increased Rashba interaction parameter, suggesting that an optimal doping density related to a maximum structural asymmetry is to be predicted.

The increased Rashba effect found by optimized Rb incorporation could explain the prolonged carrier lifetime and below band gap absorption upon Rb incorporation observed experimentally. The formation of an indirect band gap below the direct one may induce below band gap absorption and contribute to suppress carrier recombination by making the band-edge transitions spin- or momentum-forbidden; excited electrons may thus prefer to relax into the direct band edge and then radiatively recombine. The latter can explain the large expansion in carrier lifetime of RbMAFA. The dual emission can be explained in the context of the direct (intense) and indirect (weak) emission. The incorporation of Rb^+ defines the spin textures of the electronic bands by inducing Pb and I displacements that breaks the inversion symmetry as confirmed with DFT calculations. Based on these results, we attempted to make practical use of the significant Rashba splitting obtained in the Rb incorporated perovskite by designing and fabricating a hybrid photodetector using absorber layers composed of MAFA and RbMAFA crystals based absorber combined with a MoS_2 conductor. The 2D MoS_2 monolayer was successfully grown on the SiO_2/Si substrate (Figure S16), through exfoliation, to act the device photocurrent channel towards the electrodes due to its higher carrier mobilities compared to perovskites [61]. The device geometry is presented in Figure 4a and was designed based on the consideration that the perovskite SCs absorbs the incident light and produces free carriers. Then, these carriers diffuse without being recombined and transfer to the MoS_2 monolayer due to favorable energy level alignment at the perovskite/MoS_2 heterointerface (Figure 4b). Subsequently, the electrons and holes are swept by the electric field in the Ti/MoS_2 and Au/MoS_2 junctions and collected at the respective electrodes (Figure 4c). Current-voltage (I-V) characteristic curves of the RbMAFA perovskite photodetector measured under dark and upon various light intensities are shown in Figure 4d. In Figure S17b similar I-V curves under weak-light conditions are also presented. These characteristics show linear and low resistance symmetric behavior upon illumination verifying that our hybrid device works as an ultra-

sensitive broadband photodetector. The dark current was found lower than 10^{-12} A consistent with the superior crystalline quality of our perovskite. The dramatic increase in photocurrent for mild illumination conditions highlights the essential role of Rashba splitting for increased carrier generation (i.e. indirect below band gap absorption) and prolonged carrier transport in achieving high photoconductivity.

In Figure 5a the photocurrent and responsivity, which is the direct measure of the device response to light, of the RbMAFA SC perovskite photodetector under various light intensities are presented. The device responsivity R, calculated by $R=J_{ph}/L_{light}$, where J_{ph} is the photocurrent and L_{light} is the incident light intensity (see Methods), was found 2.4×10^{4} A W^{-1} that is above the to date record of 1.5×10^{4} W A^{-1} [11]. The decrease in responsivity in high light intensities is in agreement with an enhancement of many-body interactions in the lead halide perovskite that shorten the excitons and free carriers lifetime under high irradiances. Furthermore, we measured the key figure-of-merit parameter of a photodetector that is its specific detectivity (D^{*}). With the synergy of a highly boosted photocurrent due to Rashba effect and low dark current derived from the superior crystalline quality of our perovskite, we evaluated a D^{*} ~1.3×10^{18} Jones (cm $Hz^{1/2}$ W^{-1}). This value is nearly three orders of magnitude higher than the to date perovskites record of 7.5×10^{15} Jones [11], and almost five orders of magnitude higher than that of the commercially available silicon photodiodes (~3×10^{12} Jones). This remarkable performance could be the result of the intense below band gap absorption and highly prolong carrier lifetime caused by the giant Rashba splitting of our perovskite SCs. Notably, the photodetector using MAFA SC perovskite absorber exhibited inferior performance with a maximum responsivity of 0.281 W A^{-1} and maximum detectivity of $2.6\text{x}10^{10}$ Jones (Figure S17a), further corroborating the importance of using enhanced Rashba splitting in practical applications. The RbMAFA device voltage measured across the perovskite under various intensities of light in voltage detection mode and changes in the measured

voltage (ΔV) and voltage responsivity of the device at different light intensities are shown in Figure 5b,c. We estimated a high voltage responsivity of 1.9 V mW^{-1} cm^{-2}. The response speed of the device was measured by recording the current temporal photo response (Figure 5d, blue curve. The illumination power of a frequency modulated light of 532 nm laser was 0.3 mW. The green curve corresponds to the laser on-off). The rise/erase time of the present device was determined from the current transit time and found ~130 ms (Figure S17c). This is highly improved compared to previously reported polycrystalline $MAPbI_3/MoS_2$ hybrid photodetectors suggesting that it is possible to further increase the device response speed by using crystals with superior quality.

3. Conclusions

In summary, compositional engineering of perovskite single crystals provides a facile route for the generation of a large Rashba splitting in these crystals. Tailored Rb incorporation within the lattice of $MAFAPbI_3$ single crystals breaks the inversion symmetry hence inducing an experimentally estimated Rashba splitting of 104 meV. Theory predicts Rashba splitting up to 117 meV with a Rashba parameter of 1.62 eV·Å. TOF-SIMS and EDS measurements suggest that Rb is uniformly incorporated within the whole crystal lattice which means that the large Rashba splitting is not limited only on the crystals' surface. Magnetic field effect measurements verify the spin dependence in emission and photocurrent of perovskite films and devices. The compositionally engineered crystals serve as an optoelectronic material platform for the fabrication of perovskite/MoS_2 hybrid photodetector with above state-of-the art figure of merits including the highest detectivity ever reported for any type of perovskite photodetector. The perovskite compositional engineering paradigm presented here that induces the formation of large Rashba splitting provides a facile approach to realize not only record performance photodetection but also novel perovskite devices including optoelectronics and spintronics.

4. Experimental section

Materials. The organic cation salts formamidinium iodide (FAI) and methylammonium iodide (MAI) were purchased from Dyesol. The lead iodide compound was from TCI, and RbI was from abcr GmbH. All chemicals were used without further purification..

Growth of single crystal perovskite. $Rb_x(MAFA)_{1-x}PbI_3$ perovskite single crystals were grown using an inverse temperature crystallization (ITC) method with some modifications. The $MAPbI_3$ (containing 1 M MAI and PbI_2 in GBL) and $FAPbI_3$ (containing 1 M FAI and PbI_2 in GBL) solutions were mixed in a 1:1 ratio. To this mixture, 1 and 1.5 M RbI solutions (containing RbI in GBL) were added to obtain perovskites with different stoichiometries (5% RbI:$(MAFA)PbI_3$ = 5:95 (v/v), i.e., $Rb_5(MAFA)_{95}PbI_3$; 10% RbI:$(MAFA)PbI_3$ = 10:90 (v/v), i.e., $Rb_{10}(MAFA)_{90}PbI_3$; 15% RbI:$(MAFA)PbI_3$ =15:85 (v/v), i.e., $Rb_{15}(MAFA)_{85}PbI_3$). The perovskite with nominal stoichiometry $Rb_{15}(MAFA)_{85}PbI_3$ (termed as RbMAFA in this paper) gave the best photodetector performance and higher Rashba splitting. All solutions were heated at 70°C for 24 h (in ambient condition with 35–40% relative humidity) and filtered using a hydrophobic polytetrafluoethylene (PTFE-D) filter with 0.2 μm pore size. The filtrate of mixed $Rb(MAFA)PbI_3$ solution (3 mL) was stored in a convection oven at 130 °C for 6 h.

Preparation of single crystal perovskite films. The precursor single crystal solution was dropped onto the SiO_2/Si substrates and swiped linearly at a speed of 1.2 cm s^{-1} at the gap between substrates, and the blade was 80 mm. The substrates were held at *in situ* annealing during blade deposition (typically 125 °C). A 10–20 μL of precursor solution was used per 2.25 mm^2 substrate. This value was much lower than 50–100 μL typically used for spin coating of similar perovskite solutions over the same area of substrate, which demonstrated the advantages of high material usage by doctor-blade coating. After rolling was complete, the substrates were cooled immediately to avoid the possibility of thermal decomposition. All experiments were conducted under ambient conditions.

Structural and optical measurements. Perovskite thin films were characterized using an optical microscope (ICS-305B, Sometech) and a scanning electron microscope (SEM, Hitachi S4800) with an accelerating voltage of 15 kVThe optical properties were measured using a UV–visible spectrophotometer (Varian Cary 5000, Agilent Technologies) and a fluorescence spectrometer (FLSP920, Edinburgh Instruments). Steady-state PL measurements were acquired using a time correlated single photon counting setup. The samples were photoexcited using a laser head pulsed, providing <200 ps pulses with the fluence of ~30 nJ/cm^2. The PL excitation wavelength was 530 nm. The time resolved photoluminescence (TRPL) was measured using a commercial time-correlated single-photon counting system (FluoTim 200, PicoQuant). The crystallinity and elemental analysis of the thin films were determined via SAED and EDX spectrometry (AZtec software, Oxford instruments) with a transmission electron microscope (TEM, JEM 2100F, JEOL.) at an accelerating voltage of 200 kV. For preparing the TEM sample, the focused ion beam process was applied (Nova 600, Nanolab). Large-area crystallinity was measured by an X-ray diffractometer (D/MAX-2500/PC, Rigaku) using a Cu Kα source (λ=1.54Å) operated at 2.4 kW and an HR X-ray diffractometer (Smartlab, Rigaku) with a 2D detector (PILATUS 100K, Rigaku) using a Cu Kα source operating at 9 kW. For the in-plane phi scan, the 2θ angle was fixed at 14°. For the 2D XRD measurements, the X-ray analyzed area of the film was 5 mm × 5 mm. The measurement range was from 10° to 55° in the 2θ direction and from 0° to 60° in the chi direction.

Elemental analysis. The time-of-flight secondary ion mass spectroscopy (TOF-SIMS) depth profiles were collected using a TOF analyzer (TOF-SIMS 5, Ion-TOF GmbH), equipped with a 25 keV Bi^+ beam for the analysis and a 1 keV Cs^+ and O_2 source for the sputtering. TOF-SIMS images were taken TOF.SIMS.5.NSC instrument (ION.TOF Gmb) (Primary gun Bi_3^+, spectral mode: 30 keV, 30 nA, 5 μm spot size, imaging mode: 30 keV, 0.5 nA, ~120 nm spot

size). Energy dispersive spectroscopy (EDS) was conducted by using an EDS device connected to SEM.

Photodetector fabrication. Bottom-contact, top-gated FET photodetectors were constructed on Au (50 nm) electrodes (the separated spacing and width of this finger electrode were 5 μm, and the effective area was 3×10^5 μm^2) that were patterned by photolithography on a SiO_2 (500 nm)/Si (p-doped) substrate. The clean pre-patterned (in acetone, toluene and isopropyl alcohol for 15 min each, dried in an oven at 120 °C for 15 min) and exposed for 1.5 h to UV light in air SiO_2 substrate surfaces were treated with decyltrichlorosilane (DTS) for 0.5 h by immersion in 1% by volume of DTS in toluene. POCB (3 μL) was spin-coated on the SiO_2/Si-treated OTS. Monolayer MoS_2 were mechanically exfoliated from commercially available molybdenite crystals (Furuuchi Kagaku, Japan) and were later analysed using optical microscopy, Raman, and PL spectroscopy. The single crystal perovskite film was deposited on the top of the finger electrode. The samples were annealed at 80 °C for 30 min and kept under high vacuum (10^{-7} Torr) overnight (>10 h) to remove any residual solvent. The 40 nm Au electrodes were deposited on top of perovskite layer by thermal evaporation.

Electrical characterization of the photodetectors. The photodetectors were characterized using a probe station at ambient condition. A red LED (OVLBx4C7 Series, OPTEK Technology Inc., main wavelength: 623 nm) was mounted above the photodetector, which was controlled by a Keysight precision source/measure unit (B2902A) in the current source mode. The optical power density that reached the sample surface was determined by measuring a commercial reference photodiode (PDB-C154SM, Luna Optoelectronics) with a responsivity of ≈0.3 A W^{-1} at 623 nm. The single crystal photodetector response was measured with a semiconductor device analyzer B1500A (Agilent Technologies), and the overall measurement scheme was controlled via MATLAB. The extraction of the time constant was performed by modulating the LED voltage with an Agilent waveform generator (33522A) and constantly

applying 100 mV to the photodetector with the Keysight precision source/measure unit (B2902A). The voltage was applied on the photodetector top electrode. At the bottom electrode, a current amplifier (Stanford Research Systems, Model SR570) was connected, which converted the current to a voltage for the display on the oscilloscope (Agilent Technologies, MSO-X 3014A).

Magneto-effect measurements. The device for magneto-effect measurements was fabricated as follows: about 10-15 nm NiFe (Angstrom Engineering, 99.99% purity) was deposited on single crystal RbMAFA (15% Rb) using electron beam evaporation with a base chamber pressure of 1×10^{-7} Torr and deposition rate of 0.1 Å s^{-1}. Silver paste was later applied on both sides of the single crystal RbMAFA to provide electrical contact. The magneto-photocurrent measurements were carried out at room temperature. The single crystal perovskite device was transferred into a vacuum chamber that was place in a magnetic field provided by an electromagnet up to 40 mT. The magneto-photoluminescence measurements were performed using solid-state laser operating at 488 nm as a pump excitation. The MPL is defined as:

$$MPL_B = \left(\frac{PL_B}{PL_0} - 1\right)$$

and was measured at a constant laser excitation.

The magneto-electroluminescence (MEL) measurements were conducted at forward bias and the electroluminescence (EL) emission was probed with a silicon detector. The MEL is defined as:

$$MEL_B = \left(\frac{EL_B}{EL_0} - 1\right)$$

Simulations. First-principles calculations based on density functional theory (DFT) are carried out as implemented in the PWSCF Quantum-Espresso package. Geometry optimization, including dispersion correction, is performed using PBE functional, and the electrons-ions interactions are described by ultrasoft pseudo-potentials with electrons from I 5s, 5p; N, C 2s, 2p; H 1s; Rb 5s; Pb, 6s, 6p, 5d; shells explicitly included in calculations. Geometry

optimizations of 2 × 2 × 1 supercell (16 formula units) are performed with a k-point sampling of 1×1×2 by relaxing both ions and volume along with plane-wave basis set cutoffs for the smooth part of the wave functions and augmented electronic density expansions of 50 and 400Ry, respectively. GGA-SOC band structures have been considered for Rashba splitting and calculated using the method described at Ref 31.

Supporting Information

Figs S1-S17 and Tables S1-S5 about additional perovskite single crystal and MoS_2 characterization and theoretical calculations.

Acknowledgments

M.V. acknowledges support of this work by the project "Development of Materials and Devices for Industrial, Health, Environmental and Cultural Applications" (MIS 5002567) which is implemented under the "Action for the Strategic Development on the Research and Technological Sector", funded by the Operational Programme "Competitiveness, Entrepreneurship and Innovation" (NSRF 2014-2020) and co-financed by Greece and the European Union (European Regional Development Fund). A.M. and F.D.A. acknowledge European Union's Horizon 2020 research and innovation programme under Grant Agreement No. 764047 of the ESPRESSO project. The Ministero dell'Istruzione dell'Universitàe della Ricerca (MIUR) and Università degli Studi di Perugia are acknowledged for financial support through the program "Dipartimenti di Eccellenza 2018-2022" (Grant AMIS). W.J.S. and F.K.S. acknowledge the financial support from CNPq, Brazil.

References

1. S. D. Stranks, G. E. Eperon, G. Grancini, C.r Menelaou, M. J. P. Alcocer, T. Leijtens, L. M. Herz, A. Petrozza, H. J. Snaith, Science 342 (2013) 341–344.
2. T. M. Brenner, D. A. Egger, L. Kronik, G. Hodes, D. Cahen, Nat. Rev. Mater. 1 (2016) 15007.
3. D. Shi, V. Adinolfi, R. Comin, M. Yuan, E. Alarousu, A. Buin, Y. Chen, S. Hoogland, A. Rothenberger, K. Katsiev, Y. Losovyj, X. Zhang, P. A. Dowben, O. F. Mohammed, E. H. Sargent, O. M. Bakr, Science 347 (2015) 519–522.
4. Q. A. Akkerman, M. Gandini, F. Di Stasio, P. Rastogi, F. Palazon, G. Bertoni, J. M. Ball, M. Prato, A. Petrozza, L. Manna, Nat. Energy 2 (2017) 16194.
5. J. H. Heo, S. H. Im, J. H. Noh, T. N. Mandal, C.-S. Lim, J. A. Chang, Y. H. Lee, H.-J. Kim, A. Sarkar, M. K. Nazeeruddin, M. Grätzel, S. I. Seok, Nat. Photonics 7 (2013) 486–491.
6. S. D. Stranks, H. J. Snaith, Nat. Nanotech. 10 (2015) 391–402.
7. B. P. Sutherland, E. H. Sargent, Nat. Photon. 10 (2016) 295–302.
8. Z.-K., Tan, R. S. Moghaddam, M. L. Lai, P. Docampo, R. Higler, Felix Deschler, M. Price, A. Sadhanala, L. M. Pazos, D. Credgington, F. Hanusch, T. Bein, H. J. Snaith, R. H. Friend, Nat. Nanotech. 9, (2014)687–692.
9. K. Kang, H. Ahn, Y. Song, W. Lee , J. Kim, Y. Kim, D. Yoo,T. Lee, Adv. Mater. 31 (2019) 1970149.
10. J. Choi, S. Park, J. Lee, K. Hong, D.-H. Kim, C. W. Moon, G. D. Park, J. Suh, J. Hwang, S. Y. Kim, H. S. Jung, N.-G. Park, S. Han, K. T. Nam, H. W. Jang, Adv. Mater. 28 (2016) 6562.
11. J. Fing, C. Gong, H. Gao, W. Wen, Y. Gong, X. Jiang, B. Zhang, Y. Wu, Y. Wu, H. Fu, L. Jiang, X. Zhang, Nat. Electron. 1 (2018) 404–410.
12. Y. Lee, J. Kwon, E. Hwang, C.-H. Ra, W. J. Yoo, J.-H.Ahn, J. H. Park, J. H. Cho, Adv. Mater. 27 (2015) 41–46.
13. Q. Lin, A. Armin, P. L. Burn and P. Meredith, Nat. Photon., 2015, 9, 687–694.

14. L. Shen, Y. Fang, D. Wang, Y. Bai, Y. Deng, M. Wang, Y. Lu and J. Huang, Adv. Mater., 2016, 28, 10794–10800.
15. M. I. Saidaminov, V. Adinolfi, R. Comin, A. L. Abdelhady, W. Peng, I. Dursun, M. Yuan, S. Hoogland, E. H. Sargent, O. M. Bakr, Nat. Commun. 6 (2015) 8724.
16. Y. Fang, Q. Dong, Y. Shao, Y. Yuan,, J. Huang, Nat. Photon. 9 (2015) 679–686.
17. Q. Han, S.-H. Bae, P. Sun, Y.-T. Hsieh, Y. (M.) Yang, Y. S. Rim, H. Zhao, Q. Chen, W. Shi, Gang Li, Y. Yang, Adv. Mater. 28 (2016) 2253–2258.
18. L. Miao, F. Zhang, J. Mater. Chem. C 7 (2019) 1741–1791
19. I. M. Asuo, D. Gedamu, I. Ka, L. F. Gerlein, F.-X. Fortier, A. Pignolet, S. G. Cloutier, R. Nechache, Nano Energy 51 (2018) 324–332.
20. L. Dou, Y. (M.) Yang, J. You, Z. Hong, W.-H. Chang, G. Li, Y. Yang, Nat. Commun. 5 (2014) 5404.
21. B. R. Sutherland, A. K. Johnston, A. H. Ip, J. Xu, V. Adinolfi, P. Kanjanaboos, E. H. Sargent, ACS Photonics 2, 8 (2015) 1117–1123.
22. C. Xie, P. You, Z. Liu, L. Li, F. Yan, Light: Sci. Appl. 6 (2017) e17023.
23. L. Gu, Z. Fan, Light: Sci. Appl. 6 (2017) e17090.
24. H.-Y. Park, W.-S. Jung, D.-H. Kang, J. Jeon, G. Yoo, Y. Park, J. Lee, Y. H. Jang, J. Lee, S. Park, H.-Y. Yu, B. Shin, S. Lee, J.-H. Park, Adv. Mater. 28 (2016) 864–870.
25. Y. Lee, J. Kwon, E. Hwang, C.-H. Ra, W. J. Yoo, J.-H. Ahn, J. H. Park, J. H. Cho, Adv. Mater. 27 (2015) 41–46.
26. F. Bai, J. Qi, F. Li, Y. Fang, W. Han, H. Wu, Y. Zhang, Adv. Mater. Interfaces 5 (2018) 1701275.
27. C. Ma, Y. Shi, W. Hu, M. H. Chiu, Z. Liu, A. Bera, F., H. Wang, L. J. Li, T. Wu, Adv. Mater. 28 (2016)3683–3689.
28. T. Wang, B. Daiber, J. M. Frost, S. A. Mann, E. C. Garnett, A. Walsh, B. Ehrler, Energy Environ. Sci. 10 (2017) 509–515.

29. F. Zheng, L.Z. Tan, S. Liu, A. M. Rappe, Nano Lett. 15 (2015)7794−7800.

30. W. Deng, L. Huang, X. Xu, X. Zhang, X. Jin, S.-T. Lee, J. Jie, Nano Lett. 17 (2017) 2482–2489.

31. T. Etienne, E. Mosconi, F. De Angelis, J. Phys. Chem. Lett. 7 (2016) 1638−1645.

32. Y. Zhai, S. Baniya, C. Zhang, J. Li, P. Haney, C.-X. Sheng, E. Ehrenfreund, Z. V. Vardeny, Sci. Adv. 3 (2017) e1700704.

33. J. Yin, P. Maity, L. Xu, A. M. El-Zohry, H. Li, O. M. Bakr, J.-L. Brédas, O. F. Mohammed, Chem. Mater. 30, 23 (2018) 8538–8545.

34. S. B. Todd, D. B. Riley, A. Binai-Motlagh, C. Clegg, A. Ramachandran, S. A. March, J. M. Hoffman, I. G. Hill, C. C. Stoumpos, M. G. Kanatzidis, Z.-G. Yu,K. C. Hall, APL Materials 7 (2019) 081116.

35. Z. Chen, Q. Dong, Y.Liu, C. Bao, Y. Fang, Y. Lin, S. Tang, Q. Wang, X. Xiao, Y. Bai, Y. Deng, J. Huang, Nat. Commun. 8 (2017) 1890.

36. K. Frohna, T. Deshpande, J. Harter, W. Peng, B. A. Barker, J. B. Neaton, S. G. Louie, O. M. Bakr, D. Hsieh,M. Bernardi, Nat. Commun. 9 (2018) 1829.

37. Y. Chen, Y. Lei, Y. Li, Y. Yu, J. Cai, M.-H. Chiu, R. Rao, Y. Gu, C. Wang, W. Choi, H. Hu, C. Wang, Y. Li, J. Song, J. Zhang, B. Qi, M. Lin, Z. Zhang, A. E. Islam, B. Maruyama, S. Dayeh, L.-J. Li, K. Yang, Y.-H. Lo, S. Xu, Nature 577 (2020) 209–215.

38. B. Wu, H. Yuan, Q. Xu, J. A. Steele, D. Giovanni, P. Puech, J. Fu, Y. F. Ng, N. F. Jamaludin, A. Solanki, S. Mhaisalkar, N. Mathews, M. B. J. Roeffaers, M. Grätzel, J. Hofkens, T. C. Sum, Nat. Commun. 10 (2019) 484.

39. D. Niesnera, M. Hauck, S. Shresth, I. Levchuk, G. J. Matt, A. Osvet, M. Batentschuk, C. Brabec, H. B. Weber, T. Fauster, Proceedings of the National Academy of Science 115 (2018) 9509–9514.

40. N. J. Jeon, J. H. Noh, W. S. Yang, Y. C. Kim, S. Ryu, J. Seo, S. I. Seok, Nature 517 (2015) 476–480.
41. A. Amat, E. Mosconi, E. Ronca, C. Quarti, P. Umari, M. K. Nazeeruddin, M. Grätzel, F. De Angelis, Nano Lett. 14, 6 (2014) 3608–3616.
42. M. Saliba, T. Matsui, K. Domanski, J.-Y. Seo, A. Ummadisingu, S. M. Zakeeruddin, J. P. Correa-Baena, W. R. Tress, A. Abate, A. Hagfeldt, M. Grätzel, Science 2016, 354, 206.
43. G. Dresselhaus, A. F. Kip, C. Kittel, Phys. Rev. 95 (1954) 568–569.
44. E. I. Rashba, Phys. Solid State 2 (1960) 1224–1238.
45. B. Cao, L. Yang, S. Jiang, H. Lin, N. Wang, X. Li, J. Mater. Chem. A 7 (2019) 4960–4970.
46. Y. Yue, C. Wang, C. R. Grice, N. Shrestha, D. Zhao, W. Liao, L. Guan, R. A. Awni, W. Meng, A. J. Cimaroli, K. Zhu, R. J. Ellingson and Y. Yan, ACS Energy Lett. 2, 5 (2017) 1177–1182.
47. D. W. De Quilettes, S. M. Vorpahl, S. D. Stranks, H. Nagaoka, G. E. Eperon, M. E. Ziffer, H. J. Snaith, D. S. Ginger, Science 2015, 348, 683–686.
48. T. Hwang, A. J. Yun, J. Kim, D. Cho, S. Kim, S. Hong, B. Park, ACS Appl. Mater. Interfaces 11, 7 (2019) 6907–6917.
49. D. Azulay, I. Levine, S. Gupta, E. Barak-Kulbak, A. Bera, G. San, S. Simha, D. Cahen, O. Millo, G. Hodes, I. Balberg, Phys. Chem. Chem. Phys. 20 (2018) 24444–24452.
50. H. Jin, E. Debroye, M. Keshavarz, I. G. Scheblykin, M. B. J. Roeffaers, J. Hofkens, J. A. Steele, Mater. Horizon 7 (2020) 397–410.
51. V. Capozzi, Phys. Rev. B 23 (1981) 836–840.
52. W. J. Zhao, R. M. Ribeiro, M. Toh, A. Carvalho, C. Kloc, A. H. Castro Neto, G. Eda, Nano Lett. 13 (2013) 5627–5634.
53. A. Manchon, H. C. Koo, J. Nitta, S. M. Frolov, R. A. Duine, Nature Materials 14 (2015) 871–882.

54. J. Wang, C. Zhang, H. Liu, R. McLaughlin, Y. Zhai, S. R. Vardeny, X. Liu, S. McGill, D. Semenov, H. Guo, R. Tsuchikawa, V. V. Deshpande, D. Sun, Z. V. Vardeny., Nat. Commun. 10 (2019) 129.

55. C. Zhang, D. Sun, C-X. Sheng, Y. X. Zhai , K. Mielczarek3, A. Zakhidov, Z. V. Vardeny, Nature Physics 11, (2015) 427–434.

56. P. Giannozzi, S. Baroni, N. Bonini, M. Calandra, R. Car, C. Cavazzoni, D. Ceresoli, G. L. Chiarotti, M. Cococcioni, I. Dabo, A. Dal Corso, S. de Gironcoli, S. Fabris, G. Fratesi, R. Gebauer, U. Gerstmann, C. Gougoussis, A. Kokalj, M. Lazzeri, L. Martin-Samos, N. Marzari, F. Mauri, R. Mazzarello, S. Paolini, A. Pasquarello, L. Paulatto, C. Sbraccia, S. Scandolo, G. Sclauzer, A. P. Seitsonen, A. Smogunov, P. Umari, R. M. Wentzcovitch, J. Phys.: Condens. Matter. 21 (2009) 395502.

57. S. Grimme, J. Antony, S. Ehrlich, J. Chem. Phys.132 (2010) 154104.

58. J. P., Perdew, K. Burke, M. Ernzerhof, Phys. Rev. Lett. 77 (1996)3865−3868.

59. D. Vanderbilt, Phys. Rev. B 41 (1990) 7892.

60. H. J. Monkhorst, J. D. Pack, Phys. Rev. B 13 (1976) 5188−5192

61. J. Wang, Q. Yao, C. W. Huang, X. Zou, L. Liao, S. Chen, Z. Fan , K. Zhang, W. Wu, X. Xiao, C. Jiang, W. W. Wu, Adv. Mater. 28 (2016) 8302–8308.

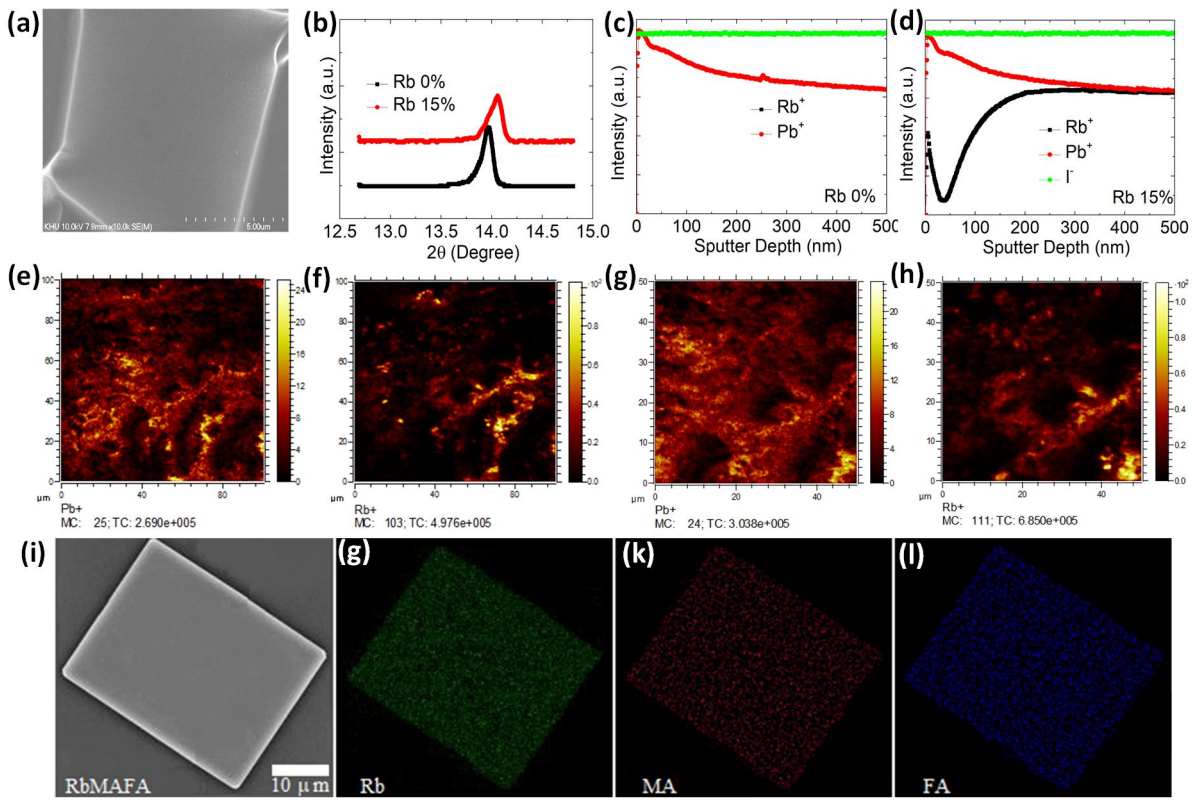

Figure 1 Structure and elemental analysis of perovskite single crystals. (a) SEM image of a typical $Rb_{0.15}(MAFA)_{0.85}PbI_3$ (15% Rb) single crystal. (b) Powder XRD patterns of MAFA (0% Rb-undoped) and RbMAFA (15% Rb-doped) perovskite single crystals. Elemental analysis of perovskite single crystals: TOF-SIMS depth profile results for (c) MAFA (10% Rb) and (d) RbMAFA (15% Rb) single crystals. TOF-SIMS imaging data for RbMAFA (10% Rb) single crystals collected on the surface (e,f) and with 50µm zoom-in (g,h). (e,g) Show the Pb^+ distribution and (f,h) the Rb^+ distribution. (i-l) EDS mapping of a representative 15% Rb RbMAFA perovskite crystal.

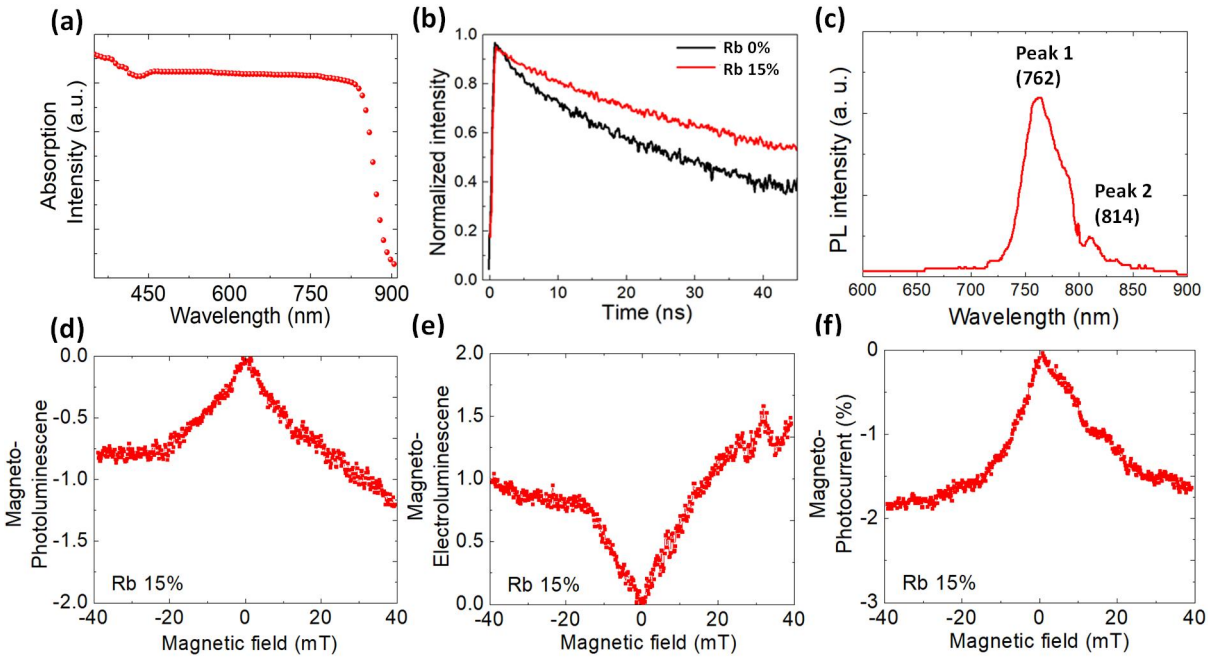

Figure 2 Optical and magnetic field dependent measurements. (a) UV-Vis absorption spectrum of 15% RbMAFA perovskite single crystals. (b) TRPL decay profiles of MAFA (0% Rb) and RbMAFA (15% Rb) perovskite single crystals. (c) Steady-state PL spectra of 0% and 155 Rb-doped perovskite single crystals. Two distinct absorption peaks one intense located at higher energy (i.e., 1.627 eV) and one weak located at higher energy (i.e., 1.523 eV) are evident. (d) Magneto-photoluminescence response of 15% Rb-doped perovskite single crystals. (e) Magneto-electroluminescence and (f) Magneto-photocurrent of a 15% Rb-doped perovskite single crystal based device.

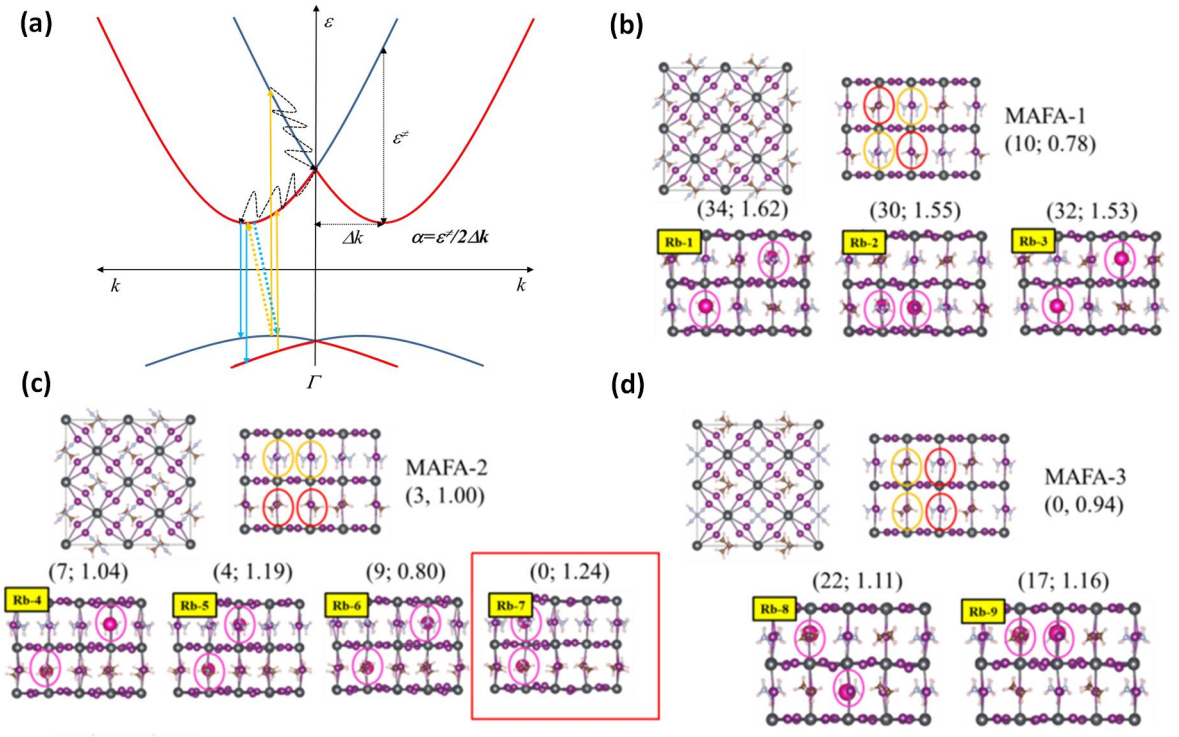

Figure 3 Rashba spin-orbit splitting. (a) Diagram of SOC-splitted Rashba bands. Both valence and conduction band are split away from the Γ point, leading to VBM and CBM which are shifted in k-space by Δk. The characteristic band energy splitting at the CBM ($\varepsilon^{\neq}$) is also shown for the conduction band. The blue and red bands correspond to the different spin channels. The orange and cyan arrows indicate absorption and emission pathways, both direct, *i.e.* preserving k (solid) and indirect (dashed). Relaxation pathways of excited electrons are shown as dashed wavy lines. The Rashba interaction parameter is defined accordingly as $\alpha=\varepsilon^{\neq}/2\Delta k$. (b-d) Modulation of the Rashba effect by structural sampling. Different configuration of $Rb_{0.12}MA_{0.44}FA_{0.44}PbI_3$ modeled by doping with 2Rb atoms in 2×2×1 supercells containing 16 formula units. For each parent MAFA structure various mutual positions of Rb cations have been explored. The values in parentheses are calculated energy difference from the most stable calculated structure in meV (0 thus corresponds to the minimum energy structure). Highlighted arethe position of representative MA and FA cations (orange and red, respectively) and of doping Rb cations (magenta).

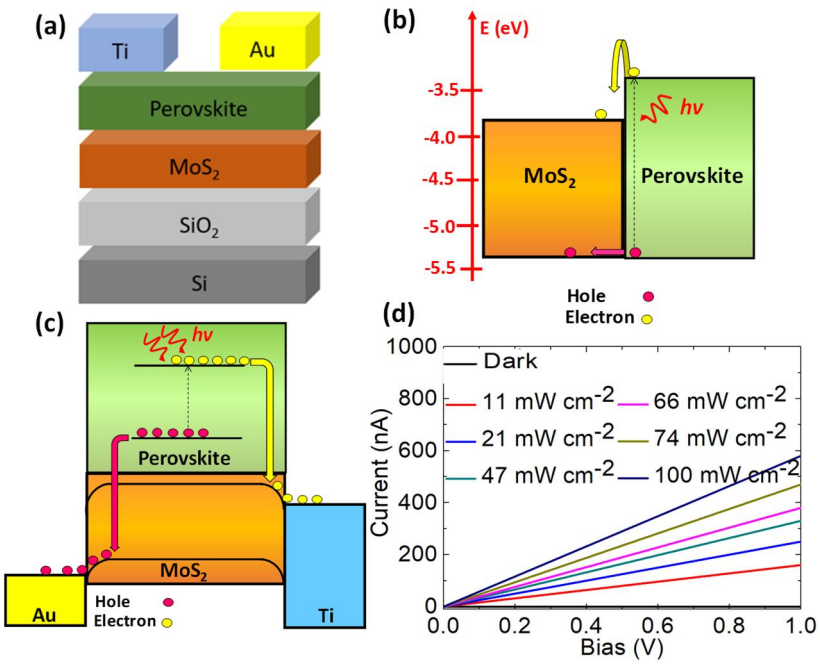

Figure 4 Photodetector configuration and working principle. (a) The device architecture of the hybrid perovskite/MoS_2 photoconductor type photodetector. (b) Schematic of energy-band diagram of the perovskite/MoS_2 interface considering vacuum level alignment before contact, and (c) illustration of the operation mechanism of the perovskite/MoS_2 hybrid photodetector under illumination. (d) I-V curves of the hybrid perovskite photodetector measured under various intensities of light.

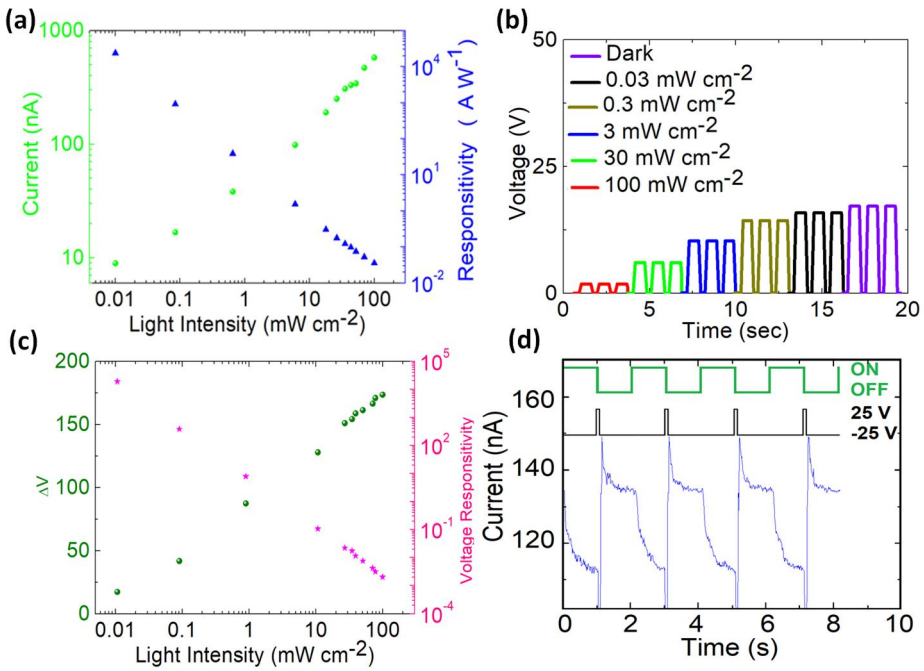

Figure 5 Performance of hybrid perovskite single crystal photodetector. (a) Photocurrent and responsivity of the photodetector under various intensities of light. (b) Photodetector device voltage measured across the perovskite under various intensities of light in voltage detection mode. (c) Change in the measured voltage (ΔV) and voltage responsivity of the device at different light intensities. (d) Temporal photoresponse of the perovskite photodetector (blue curve). The illumination power is 0.3 mW and the laser wavelength is 532 nm. The laser on-off (green curve) is controlled by a mechanical shutter synchronized with the reset back gate voltage pulses (black curve).